Crystallinity, Magnetic and Electrical Properties of Bi doped LaVO₃

by

Sepiedeh Pirasteh

M.Sc, University of Pune, 2009

B.Sc, Ferdowsi University of Mashhad, 2006

A THESIS SUBMITTED IN PARTIAL FULFILMENT OF
THE REQUIREMENTS FOR THE DEGREE OF

MASTER OF SCIENCE

in

The Faculty of Mathematics and Science

Department of Physics

BROCK UNIVERSITY

April, 2012

In presenting this thesis in partial fulfillment of the requirements for advanced degree at Brock University, I agree that the Library shall make it freely available for reference and study. I further agree that permission for extensive copying of this thesis for scholarly purposes may be granted by the head of my department or by his or her representatives. It is understood that copying or publication of this thesis for financial gain shall not be allowed without my written permission.

. . . .

(Signature)

Department of Physics
Brock University
St. Catharines, Canada

Date . . . .

Abstract:

We report the results of crystal structure, magnetization and resistivity measurements of Bi doped $LaVO_3$. X-ray diffraction (XRD) shows that if doping Bi in the La site is less than ten percent, the crystal structure of $La_{1-x}Bi_xVO_3$ remains unchanged and its symmetry is orthorhombic. However, for higher Bi doping (>10%) composite compounds are found where the XRD patterns are characterized by two phases: $LaVO_3+V_2O_3$. Energy-dispersive analysis of the x-ray spectroscopy (EDAX) results are used to find a proper atomic percentage of all samples. The temperature dependence of the mass magnetization of pure and single phase doped samples have transition temperatures from paramagnetic to antiferromagnetic region at $T_N=140$ K. This measurement for bi-phasic samples indicates two transition temperatures, at $T_N=140$ K ($LaVO_3$) and $T_N=170$ K (V_2O_3). The temperature dependence of resistivity reveals semiconducting behavior for all samples. Activation energy values for pure and doped samples are extracted by fitting resistivity versus temperature data in the framework of thermal activation process.

Table of Contents

List of Figures:

List of the Tables:

Acknowledgments

I sincerely thank various people for their scientific and technical contributions, kind support, and encouragement throughout my M.Sc course work and research project. First and foremost, I thank Prof. F.S. Razavi, my research supervisor, for his mentorship and constant encouragement throughout this project. I appreciate all contributions of his time, ideas, and suggestions during last two years. I want to acknowledge and thank Dr. M. Singh for his valuable advise and friendly help. I very much appreciate his enthusiasm, willingness, genius ability in leading my research project. My warm thank to Prof. R.K. Kremer, Max Planck Institute, for EDAX measurement. I am very grateful to Prof. D.A. Crandles and Prof. B. Mitrovic for their inspirational discussion, thesis correction and helpful comments as my research committee members. I thank the technical staffs at the machine and electronic shop, and glassblower for their constant help in troubleshooting and fabricating the required components in my research.

I am also thankful for other past and present group members and grad students. In particular I thank my lab colleagues, J. Korobanik, B. Indovski and M. Taheri, for their assistance during my work in the lab. I thank J. Manson and M. Przedborski for their valuable contributions to my personal and professional time at Brock.

I gratefully acknowledge the Brock University, NSERC, CFI, Ministry of Research and innovation-Ontario for financial support. My time at Brock was made enjoyable due to the many friends and group that became a part of my life. I am grateful for time spent with friends, and for other people and memories.

Last, but most importantly, I express my gratitude to my family. I can not thank them enough for their affection, encouragement and support during these past two years. Although they are living far away, I couldn't have done it without them.

Chapter 1

Introduction

Metal oxides, including perovskite-type related oxides (ABO_3) have many interesting properties which have been widely researched and studied [1-8]. These extraordinary properties lead to their applications in various electronic devices, optoelectronic devices and storage media [2]. Further, they are also potential candidates in emerging electronic and spintronic technologies e.g. metal-oxide transistors (MOS), magnetic random access memories (MRAMs), and discs or tapes for information storage [3].

Among the perovskites, orthovanadate is one of the important transition metal oxide groups with chemical formula of RVO_3. The orthovanadates are semiconducting or insulating. As an example, $LaVO_3$ and YVO_3 are Mott insulators, but they become metallic by carrier doping [4]. All the orthovandates have pseudo-cubic symmetry and paramagnetic ordering at room temperature [4-6]. At low temperature, they show antiferromagnetic behavior which is influenced by structural phase transitions [4]. Past studies show that it is possible to control the antiferromagnetic to paramagnetic transition temperature (Néel temperature, T_N) by choosing the appropriate rare-earth elements at R site [5-7]. These rare-earth elements are shown in Table 1.1. The phase diagram of orthovanadates for variation of Néel temperature T_N as a function of ionic radius (IR) of rare-earth elements, as reported in literature [5-8], is plotted in Fig. 1.1. It shows that the value of T_N decreases significantly as we move across La to Lu rare-earth elements in periodic table. For example, the change in the value of T_N from La^{3+} to Lu^{3+} is as large as 30% while a change in value of ionic radius is only 15% [5-8]. The decreasing ionic radius of R^{3+} cation contracts the unit-cell of orthovanadates. This contraction further induces compressive stress to the V-O-V bond length and bond angle. This ultimately tilts the VO_6 array and increases the distortion to the pseudo cubic unit-cell of RVO_3 [4, 9].

Unlike the other members of the orthovanadates, $LaVO_3$ has a higher structural transition temperature and a large ionic radius at R site, leading to almost cubic symmetry. These special properties of $LaVO_3$ have potential applications. Hence, many research works have been carried out both in the experimental and the theoretical field. These demonstrate the importance of the structural and physical properties of $LaVO_3$. Further, these properties can be varied by growing non-stoichiometric or doped $LaVO_3$ in either polycrystalline, single-crystal or thin film form [1].

The crystal structure of $LaVO_3$ compound has been studied as a function of temperature. Bordet *et al.* [10] reported the crystal symmetry of $LaVO_3$ compound changes below room temperature (about 140 K). Their results show that the structure of $LaVO_3$ changes from orthorhombic symmetry at room temperature (a=5.555, b=7.748, c=5.553 Å) and space group *Pnma* to monoclinic symmetry and space group $P2_1/a$ with the cell parameters a=5.594, b=7.759, c=5.565 Å. This symmetry distortion of $LaVO_3$ is accompanied with a transition from antiferromagnetic to paramagnetic behavior at 140 K [10]. As a consequence, the distortion in octahedral VO_6 and V-O-V bond length and bond angle accompanies the structural and magnetic phase transition at $LaVO_3$ compounds [10]. $LaVO_3$ is Mott insulator [11] and shows semiconductor-like behavior at high temperature with energy gap about E_g=1.1 eV [12].

Seim *et al.* [13] studied the structural properties of non-stoichiometric $La_{1-x}VO_3$. Their results show the unit-cell dimensions of $La_{1-x}VO_3$ decrease by increasing x as the structural distortion increases by increasing La deficiency in $La_{1-x}VO_3$. The oxidation state of V enhances with an average value between +3.00 and +3.51 for $0.00 \leq x \leq 0.17$. The multiple oxidation states of vanadium change the V-O bond lengths from 200.2 pm for $LaVO_3$ to 198.0 pm for $La_{0.90}VO_3$ [13]. Seim *et al.* also studied the temperature dependence of the magnetic susceptibility of $La_{1-x}VO_3$. As shown in Fig. 1.2 (a), Néel temperature decreases from 140 K for $LaVO_3$ to 70 K for $La_{0.92}VO_3$. However, for the $La_{0.90}VO_3$ a paramagnetic behavior is observed with no observation of structural and magnetic transition as shown in Fig. 1.2 (a) [13, 14].

Gharetape *et al*. [15] reported the properties of LaV_xO_3. The crystal symmetry remains unchanged and free from impurity phases for LaV_xO_3 for $0.92 \leq x \leq 0.98$. However, the lattice parameters of LaV_xO_3 increase by decreasing x from 1 to 0.92 accompanied by multiple oxidation states of vanadium of V^{3+} and V^{4+} [15]. On the other hand, the value of magnetic transition temperature for the vanadium deficient compounds remains unchanged from that of the $LaVO_3$ as shown in Fig. 1.2 (b). They also measured the temperature dependence of resistivity for V deficient LaV_xO_3 compounds (Fig. 1.3 (b)). They reported a semiconductor behavior with increasing in activation energy as the V deficiency increased in LaV_xO_3 [15].

The doping of Sr and Ca cations at La site in $LaVO_3$ enhances the oxidation state of V, because of different oxidation state of Ca^{2+} and Sr^{2+} in comparison to La^{3+}. Substitution of Ca at La site does not change the crystal structure significantly, as the ionic radius of Ca^{2+} {1.14 Å} is very close to that of La^{3+} {1.17 Å}, unlike the Sr doping at La site [16]. Dougier and Hagenmuller [17] reported three different structures, tetragonal, orthorhombic, and hexagonal. They obtained these differences in symmetries for different ranges of Sr doping ($0.6 \leq x \leq 1.0$). The difference between the ionic radius of La^{3+} {1.17 Å} and Sr^{2+} {1.32 Å} causes these structural changes. The magnetic susceptibility of doped $LaVO_3$ is quite different from the deficient compounds. The works done by Mahajan *et al*. [18] on $La_xSr_{1-x}VO_3$ compounds exhibit decreasing susceptibility and antiferromagnetic phase transition temperature with increasing Sr content. A similar magnetic properties are also observed in $La_{1-x}Ca_xVO_3$ [16] Fig. 1.2 (c, d). Temperature dependence of resistivity in $La_{1-x}Sr_xVO_3$ shows metallic behavior by doping more than x=0.2 [12]. Resistivity measurements performed for $La_{1-x}Ca_xVO_3$ by Maiti and co-workers, show a similar metal-insulator (M-I) transition for doping of x > 0.3 [15]. These results are shown in Fig. 1.3 (c, d). The M-I transition is explained by presence of strong electron-electron interaction and charge transfer through the multiple oxidation states of V ions in the V^{3+}-O-V^{4+} bonds [11, 16].

Similar to carrier doping, the epitaxial growth of $La_{1-x}Sr_xVO_3$ thin films may affect the structural phase transition, because of the strain effect. Lekshmi *et al*. [19] studied the changes in crystal structure of $La_{1-x}Sr_xVO_3$ thin films. Their results show the

decreasing of the cell parameters by increasing Sr content. The incorporation of Sr^{2+} ions in the La^{3+} sites of $La_{1-x}Sr_xVO_3$ thin films leads to the partial conversion of oxidation state of vanadium from the greater ionic radius of V^{3+} (=0.64 Å) ions to the smaller ionic radius of V^{4+} (=0.54 Å) ions. These average V oxidation states and compressive strain effects accompany to the contraction of lattice parameters in $La_{1-x}Sr_xVO_3$ thin films. The rotation of VO_6 octahedron increases the V-O-V bond angle in $La_{1-x}Sr_xVO_3$ thin films [19, 20]. Dao *et al.* [21] also reported the strain effect of $LaAlO_3$ on the $La_{0.75}Sr_{0.25}VO_3$ thin films. The decreasing of the film thickness reduces the lattice parameter (c-axis), because of the increasing of octahedral VO_6 rotation as a consequence of epitaxial growth. The electrical behavior of $La_{1-x}Sr_xVO_3$ thin films on $LaAlO_3$ substrate is in close agreement with bulk $La_{1-x}Sr_xVO_3$ [18, 19]. The $La_{1-x}Sr_xVO_3$ thin films remain insulators for doping range $0.1 \leq x \leq 0.175$. However, the electrical behavior significantly changes from $0.2 \leq x \leq 0.42$ range, and the film remains metallic in the whole temperature range, as shown in Fig. 1.3 (d) [9, 19].

From the above discussion on properties of $LaVO_3$, it is clear that the properties of $LaVO_3$ are sensitive to the three important factors: (i) composition, (ii) crystal structure, and (iii) chemical pressure (i.e. chemical doping). The purpose of this research project is based on the study of the structure, magnetic, and electrical properties of Bi doped $LaVO_3$. We chose bismuth as the doping element because its oxidation state and ionic radius are approximately the same as that of Lanthanum ions (La^{3+}=1.16 Å and Bi^{3+}=1.17 Å) [22]. Thus, we expect to see no changes in the structural symmetry and oxidation states of V site by doping Bi. Further, the atomic configuration Bi^{3+} is $[Xe]4f^{14},5d^{10},6s^2$. The Bi^{3+} has two extra electrons (lone-pair electron) which are not chemically bonded to the other atoms in the lattice. It was speculated that the effect of $6s^2$ electrons at the La site, may produce interesting structural and physical properties for $LaVO_3$. The atomic number of bismuth (Z=83) is higher than lanthanum (Z=57). It is clear, the number of protons in Bi are higher than La. Therefore, Bi has more tendency to attract electrons than La (electronegativity). These two factors, lone-pair electron and higher electronegativity of Bi^{3+} than La^{3+}, can change the V-O bond length and bond angle by inducing stress and chemical pressure to the lattice by doping Bi. In our study,

we have attempted to understand the different magnetic and electrical properties produced by this particular chemical doping and furthermore will consider other factors involved for these properties.

The outline of my thesis is as follows:

- Chapter 2 presents the general structure, magnetic and electrical properties of orthovanadates in detail by presenting theoretical models to understand and analyze our measurements.

- Chapter 3 deals with the details of the measurement techniques and systems used for this project.

- Chapter 4 reports the results and discussions of the given data.

- Chapter 5 summarizes the purpose and conclusion of this work.

1	Atomic Number													
2	Rare-earth ions													
3	Valence electron shell of rare-earth ions													
1	57	58	59	60	61	62	63	64	65	66	67	68	69	70	71
2	La^{3+}	Ce^{3+}	Pr^{3+}	Nd^{3+}	Pm^{3+}	Sm^{3+}	Eu^{3+}	Gd^{3+}	Tb^{3+}	Dy^{3+}	Ho^{3+}	Er^{3+}	Tm^{3+}	Yb^{3+}	Lu^{3+}
3	$4f^0$	$4f^1$	$4f^2$	$4f^3$	$4f^4$	$4f^5$	$4f^6$	$4f^7$	$4f^8$	$4f^9$	$4f^{10}$	$4f^{11}$	$4f^{12}$	$4f^{13}$	$4f^{14}$

Table 1.1 Periodic table for rare-earth $4f^n$ ions series.
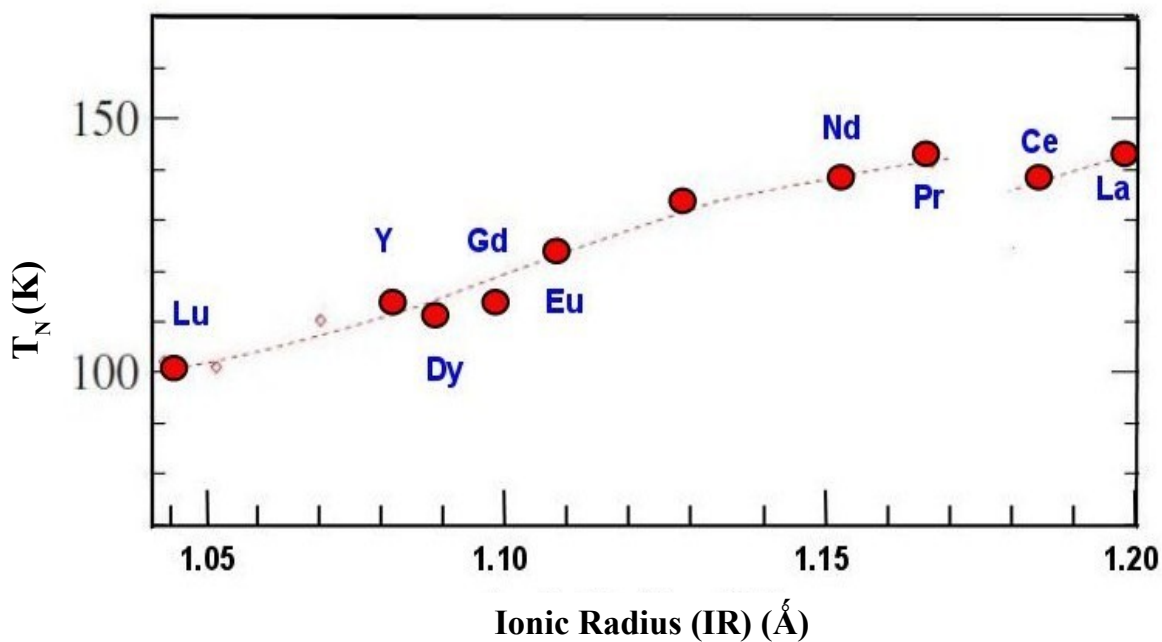
Figure 1.1 Paramagnetic to antiferromagnetic transition temperature of orthovanadates (T_N) versus ionic radius (IR) of rare-earth $4f^n$ ion series, showing decreasing Néel temperature by decreasing ionic radius from 140 K to 100 K, adopted from Ref. [5-8].
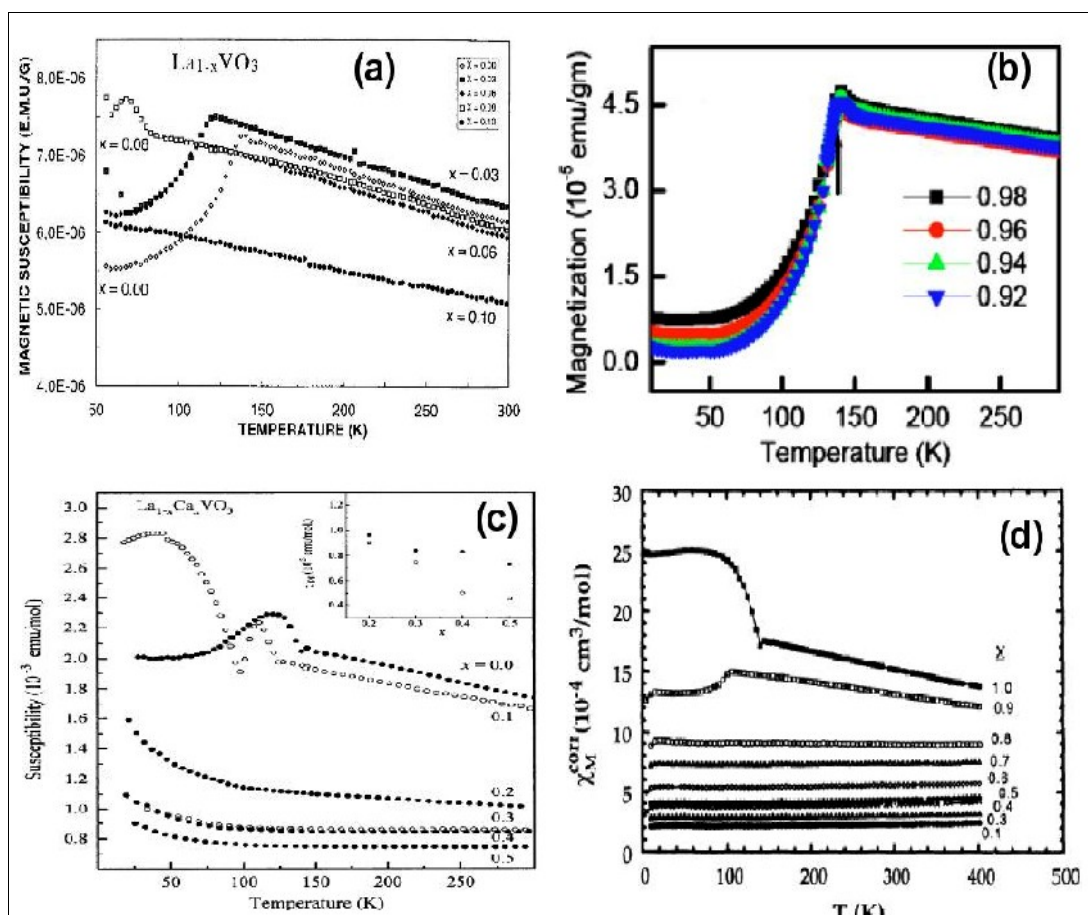
Figure 1.2 Mass magnetization versus temperature of (a) $La_{1-x}VO_3$, adopted from Ref. [13] and (b) LaV_xO_3, adopted from Ref. [15]. Molar susceptibility and molar magnetization versus temperature of (c) $La_{1-x}Ca_xVO_3$, adopted from Ref. [16] and (d) $La_xSr_{1-x}VO_3$, adopted from Ref. [18]. x values are indicated in each panel. The conversion of unites are given in Table 1.2.

Quantity	symbol	cgs unit	SI unit	Gaussian unit
Mass susceptibility	χ_g	emu/g	$4\pi \times 10^{-3}$ m^3/kg	4π cm^3/g
Molar susceptibility	χ_m	emu/mol	$4\pi \times 10^{-6}$ m^3/mol	4π cm^3/mol

Table 1.2. Table of unit conversions for the magnetic susceptibility.
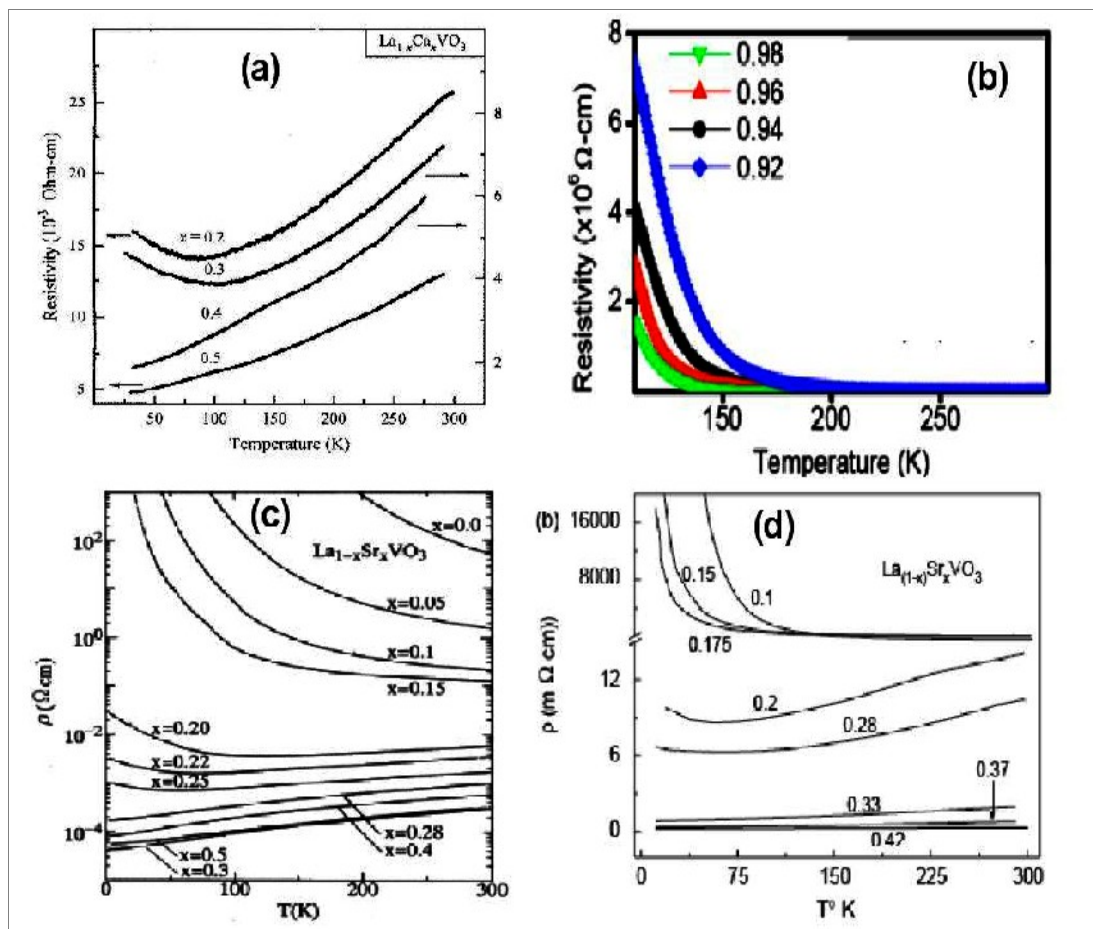
Figure 1.3 Resistivity versus temperature of (a) $La_{1-x}Ca_xVO_3$, adopted from Ref. [16] (b) $LaV_{1-x}O_3$, adopted from Ref. [15] (c) $La_{1-x}Sr_xVO_3$, adopted from Ref. [11] and (d) $La_{1-x}Sr_xVO_3$ thin films on $LaAlO_3$ substrate, adopted from Ref. [19]. x values are indicated in each panel.

Chapter 2

Properties of orthovanadates

2.1 Crystal structure

In order to interpret the properties of orthovanadates, it is critical to understand their crystal structure in detail. The unit cell of an ideal perovskite RVO_3, where R is usually a trivalent rare earth cation, is shown in Fig. 2.1. As illustrated, the large cations (R^{3+}) are located at the corner of the cubic unit cell, the small cation (V^{3+}) is at its center position, and the O^{2-} ions are located at face-centered position. In these oxides, V^{3+} is in $3d^2$ electronic configuration [2].

The structural distortion of RVO_3, as shown in Fig. 2.2, is increased by tilting of unit cells along the crystallographic axis from $LaVO_3$ to $LuVO_3$, causing the system to adopt from almost cubic pervsokite symmetry to an orthorhombic symmetry. In contrast to $LaVO_3$, by choosing appropriate rare earth elements at R site, the structural transition temperature and ionic radius of orthovanadates can decrease as much as 30% [7, 8]. These changes are a consequence of smaller ionic radius [3]. Substituting rare earth ions at R site, with smaller ionic radius than La, induces compressive stress to the crystal structure. Therefore the octahedral VO_6 tilts and changes the bond angle of V-O-V and the bond length of R-O and V-O bonds. Thus, the structure becomes distorted [9]. The variation of the bond angle ($\Delta\theta$) of V-O-V bonds from perfectly aligned angle of 180°, increases as ionic radius decreases. The bond angle of V-O-V is expressed by $\theta = 180°-\Delta\theta$. As reported by Martínez-Lope *et al.* [4], the $\Delta\theta$ is 11.6° for La^{3+} and this value increases to $\Delta\theta=19.1°$ for Lu^{3+}. Clearly the higher ionic radius of R ion of orthovanadates can elongate the V-O-V bonds at higher bond angle θ [2, 3].

Past studies show that $LaVO_3$ crystallizes in different crystal symmetry. According to these studies, it possesses an orthorhombic crystal symmetry at room temperature (300 K) while it adopts to monoclinic symmetry at 140 K which is also the Néel temperature (T_N). Typical orthorhombic and cubic unit cell of $LaVO_3$ are shown in Fig. 2.2 (a) and (b), respectively.
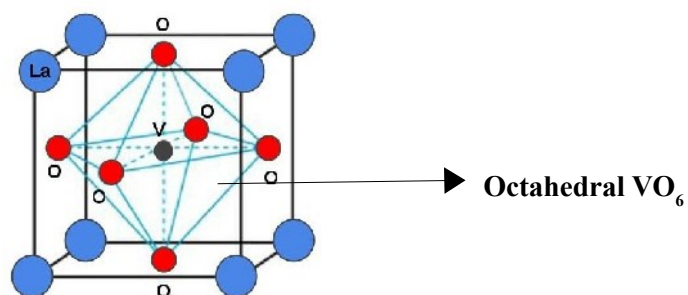
Figure 2.1 A typical unit cell of perovskite crystal RVO_3, showing the octahedral VO_6 array within unit cell, R=La ions with larger circle, and V ion with smaller circle that are surrounded by oxygen ions.
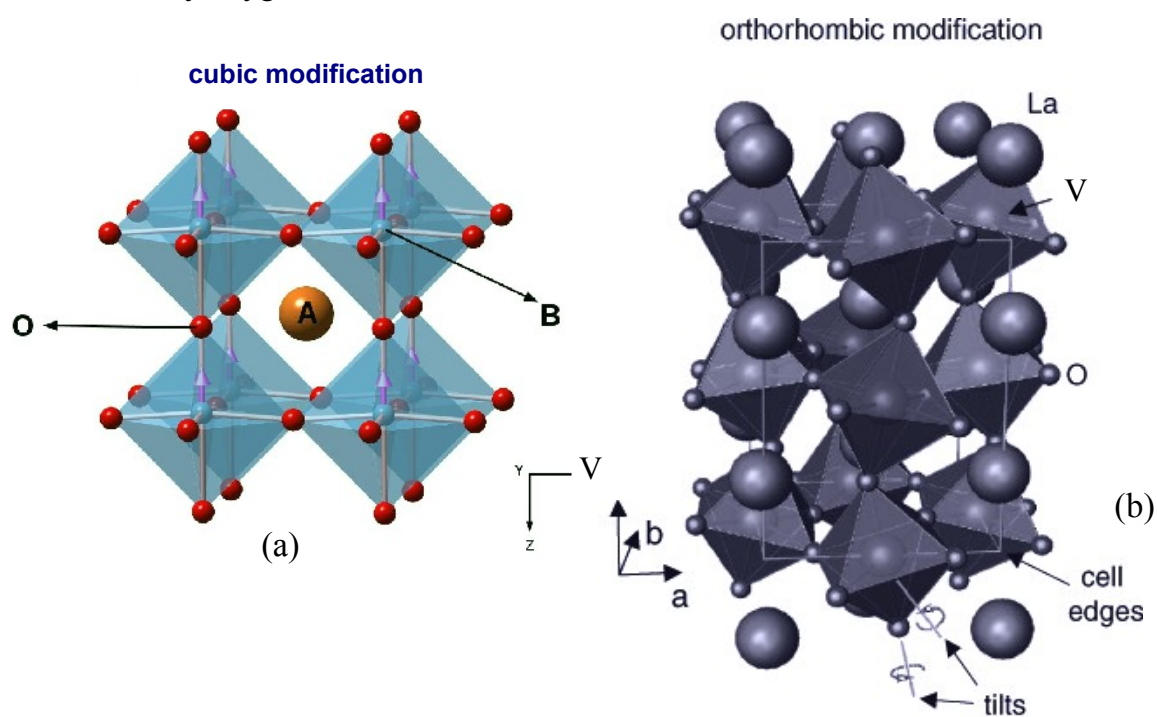
Figure 2.2 Schematic of crystal structure of perovskites, showing (a) cubic symmetry, adopted from *CrystalMaker 2.3*, file section for *BaTiO₃* and (b) orthorhombic symmetry, adopted from Ref. [23].

2.2 Magnetic properties

In the Bohr model of an atom, an electron rotates in the circular path around the nucleus which induces a current loop. This current produces a magnetic field due to magnetic dipole moment of size [2, 24]

$$\vec{\mu}_l = IA = (ef)(\pi r^2).\tag{2.1}$$

Where I is the current of the orbiting electron, A is the area of the circular path with radius of r, e is the charge of the electron, and f is the frequency of rotation around the nucleus that produces the magnetic field [24]. The orbiting electron with mass m_e and tangential velocity of v produces the orbital angular momentum [24]. The relation between magnetic dipole moment and orbital angular momentum is given in

$$\vec{L} = \vec{r} \times \vec{p} = r m_e v = r m_e (2 \pi r f) = r m_e \left(-2\frac{\vec{\mu}_l}{er}\right) = -2\frac{m_e}{e}\vec{\mu}_l\tag{2.2}$$

$$\vec{\mu}_l = -\frac{e}{2 m_e}\vec{L} \qquad\qquad |\vec{\mu}_l| = \frac{e}{2 m_e}\sqrt{L(L+1)}\,\hbar\tag{2.3}$$

In addition to orbital angular momentum, the electron also possesses an intrinsic spin angular momentum that generates an additional spin magnetic moment μ_s

$$\vec{\mu}_s = -\gamma\frac{e}{2 m_e}\vec{S} \qquad\qquad |\vec{\mu}_s| = \gamma\frac{e}{2 m_e}\sqrt{S(S+1)}\,\hbar\tag{2.4}$$

The quantity γ is gyromagnetic ratio. For the electron, its value is about $\gamma = 2.00$. The total angular momentum (J) is a sum of spin and orbital angular momentum where the vector relation is defined as $J = L + S$. Similarly, the total magnetic moment vector is expressed as $\mu = \mu_l + \mu_s$

$$\vec{\mu} = -\frac{e}{2 m_e}(\vec{L} + 2\vec{S}) \qquad\qquad |\vec{\mu}_J| = \left(\frac{-e\hbar}{2 m_e}\right)\sqrt{J(J+1)}\,g\tag{2.5}$$

where quantity g is called spectroscopic splitting factor [24, 25].

$$g = 1 + \frac{J(J+1) + S(S+1) - L(L+1)}{2 J(J+1)}.\tag{2.6}$$

If the magnetic dipole moments of each atom are placed in an external magnetic field B, the interaction energy of the magnetic moments with applied field is quantized [8]. This energy splitting of an atom in a external (applied) magnetic field B is explained by "Zeeman effect", as given by Hamiltonian operator [26]

$$H = -\vec{\mu}_J \cdot \vec{B} = -\frac{e}{2m_e} g \vec{J} \cdot \vec{B}.$$
(2.7)

The energy eigenvalue of this operator is equal to

$$E_{m_J} = -\frac{e}{2m_e} g \hbar m_J B$$
(2.8)

Where $m_J = J, J-1,...,-J+1, -J$.

The total magnetic dipole moments of N atoms per volume unit are defined as magnetization.

$$\vec{M} = \sum \frac{\vec{\mu}_i}{V} = N \frac{g^2 \mu_B^2 J(J+1)}{3 k_B T} \vec{B},$$
(2.9)

where B is applied magnetic field, T is temperature, J is total angular momentum quantum number, and $\mu_B = e\hbar/2m_e$ is the Bohr magneton [2, 24, 25, 26]. The response of the total magnetic dipole moment to the applied magnetic field causes various magnetic behaviors in different materials. Magnetic materials can be grouped in five different types [2, 3] as follows:

Diamagnetic materials are the type of materials which do not have a permanent magnetic moment. By applying magnetic field, the interaction between dipole moments and external field orient the magnetic moments exactly opposite direction to the applied field which induces negative magnetization.

In paramagnetic materials the orientations of magnetic moments are random. Therefore, by applying a magnetic field, a small fraction of the moments align to applied field direction. The magnetization is positive and small. Because the exchange interaction between dipoles is almost zero large magnetic field should be applied for partial alignments of magnetic moments.

Ferromagnetic solids have permanent magnetic moments that are naturally aligned. Most of the magnetic moments align parallel to the direction of applied field causing very large and positive magnetization. Interactions between the magnetic moments are strong. Thus, by applying small magnetic field, large net magnetization is induced in the material.

In antiferromagnetic materials the interaction between magnetic moments align the moments anti-parallel to each other. These materials can be considered as two identical sub-lattices of same magnetic ions, but with anti-parallel orientation of magnetic moments which exactly cancel out. Therefore, the net magnetic moment is zero.

Ferrimagnetic materials have two sub-lattices of aligned anti-parallel moments. The ferrimagnets are microscopically similar to the antiferromagnetic materials. The sub-lattices have opposite magnetic moment alignment to each other. But the net magnetization of ferrimagnets is a non zero value because of the different magnitudes of the magnetic moments in the two sub-lattices. These materials have large positive or negative susceptibility. The magnetic dipole moment alignments and variation of the magnetization by applied field are shown in Fig. 2.3 for magnetic materials.
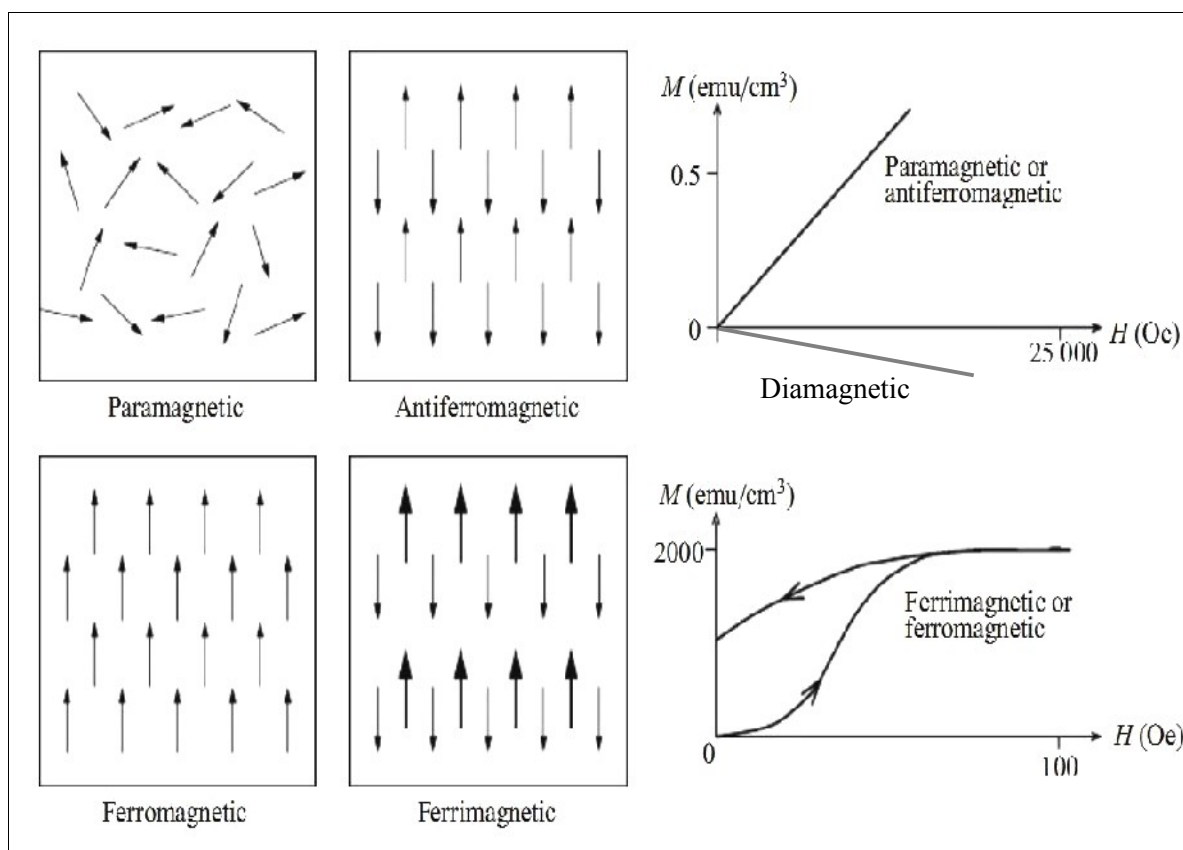
Figure 2.3 Ordering of the magnetic dipole moments in the different types of magnetic materials. The magnetization versus magnetic field graphs are shown for magnetic materials, adopted from Ref. [2].

2.2.1 Temperature dependence of susceptibility (Curie-Weiss Law)

The magnetization of a material is defined as the total magnetic moment per unit volume. Due to the interaction of magnetic moments with the external field the magnetization can be varied. The response of the magnetic moments to the applied field (H) is called susceptibility, given in Eqn. 2.10 [2].

$$\chi = \frac{M}{H} \tag{2.10}$$

The magnetic susceptibility is generally expressed as $\chi = \chi_d + \chi_{orb} + \chi_{dia}$ which is the sum of the interaction between d-spin (transition metal ions), orbital paramagnetism (induced magnetic field from unpaired electrons) and diamagnetism (the magnetic field generated by paired electrons in inner shells), respectively [12]. The unit of susceptibility in SI unit is dimensionless and in cgs units is emu/cm^3. Weiss localized moment theory is described for three kind of magnetic materials that are antiferromagnets, paramagnets and ferromagnets. This theory shows the temperature dependence of the susceptibility above the appropriate magnetic transition temperature to be: [2, 3]

$$\chi = \frac{M}{H} = \frac{C}{T + \Theta} \quad . \tag{2.11}$$

Here Θ is the Weiss temperature and C is the Curie constant. The value of Θ is different for each magnetic material. For ferromagnets $\Theta > 0$ and $\Theta = T_c$, where T_c is a critical temperature for ferromagnetic material is called Curie temperature (T_c). Below this temperature the moments order ferromagnetically. For antiferromagnets, the spin of magnetic moments disorder above the Néel temperature (T_N) and below this temperature the moments have antiparallel spin orientation. Θ is negative and $T_N \neq \Theta$. For paramagnets, there is no transition temperature and $\Theta = 0$. Different values for Weiss temperature are shown in Fig. 2.4 (a), which illustrates inverse susceptibility versus temperature. The curve of susceptibility versus temperature for an antiferromagnet shown in Fig. 2.4 (b) has a sharp cusp and a maximum value at T_N [2, 25].

At T=0 K, the moment can easily align with applied magnetic field H, but at higher temperature thermal energy randomizes the moment alignment and the effective

magnetic moment decreases [27]. The temperature dependence of the susceptibility of effective magnetic moments in cgs units is given in Eqn. 2.12 [25].

$$\chi = \frac{C}{T - \Theta} = \frac{N g^2 J(J+1) \mu_B^2}{3 k_B (T - \Theta)} = \frac{N \mu_{eff}^2 \mu_B^2}{3 k_B (T - \Theta)} \tag{2.12}$$

Here the number of magnetic ions, g-factor, Bohr magneton, effective magnetic moment, total angular momentum and Boltzman constant are N, g, μ_B, μ_{eff}, J and k_B, respectively [2, 27]. The effective magnetic moment of an atom with total spin and orbital angular momentum in the unit of Bohr magneton number is defined as $\mu_{eff} = g \sqrt{J(J+1)}$. The magnitude of the effective magnetic moment can be obtained from paramagnetic susceptibility region [27].

The effective magnetic moment (μ_{eff}), Curie-constant per unit of mass (C_g), Curie-Weiss temperature (Θ) can be found by linear fitting of inverse susceptibility ($1/\chi$) graph versus temperature, from Néel to room temperature [2].

$$\chi = \frac{M}{H} = \frac{C_g}{T - \Theta} \qquad \longrightarrow \qquad \frac{1}{\chi} = \frac{H}{M} = \frac{T}{C_g} - \frac{\Theta}{C_g} \tag{2.13}$$

The slope of Eqn. 2.13 is $(C_g)^{-1}$ and the intercept represents Θ/C_g. Magnetic moment also can be calculated by the following equations [28].

$$C_g = \frac{g^2 J(J+1) \cdot \mu_B^2}{3 k_B} \cdot \frac{N}{m} \tag{2.14}$$

$$C_g = \frac{\mu_{eff}^2 \cdot \mu_B^2}{3 k_B} \cdot \frac{N}{m}$$

$$\mu_{eff} = \sqrt{\frac{3 k_B}{\mu_B^2} \cdot \frac{m}{N}} \cdot \sqrt{C_g} \tag{2.15}$$

$$n = \frac{m}{M_m} \qquad \text{and} \qquad N = n \cdot N_A \qquad \longrightarrow \qquad \frac{N}{m} = \frac{n \cdot N_A}{n \cdot M_m} = \frac{N_A}{M_m}$$

$$\mu_{eff} = \sqrt{\frac{3k_B}{\mu_B^2} \cdot \frac{M_m}{N_A}} \cdot \sqrt{C_g} \tag{2.16}$$

Here N_A is the Avogadro number $= 6.02 \times 10^{23}$, M_m is the molecular mass, and k_B is the Boltzmann's constant $= 1.38 \times 10^{-16}$ erg/K. The simple form of the effective magnetic moment (μ_{eff}) is usually in the number of Bohr magneton in Eqn. 2.8 ($\mu_B = 0.927 \times 10^{-20}$ erg/Oe) in cgs units [29].

For the multi-phase materials, the Eqn. 2.16 should be modified. For example for a bi-phasic sample, the equations are changed to the following two expressions:

$$M'_m = (x)M_{m(phase\,1)} + (1-x)M_{m(phase\,2)} \tag{2.17}$$

Here M'_m is combined molecular mass of two phases, x is the amount of the concentration of each phase.

$$\mu'_{eff} = \sqrt{\frac{3k_B}{\mu_B^2} \cdot \frac{M'_m}{N_A}} \cdot \sqrt{C_g} \tag{2.18}$$
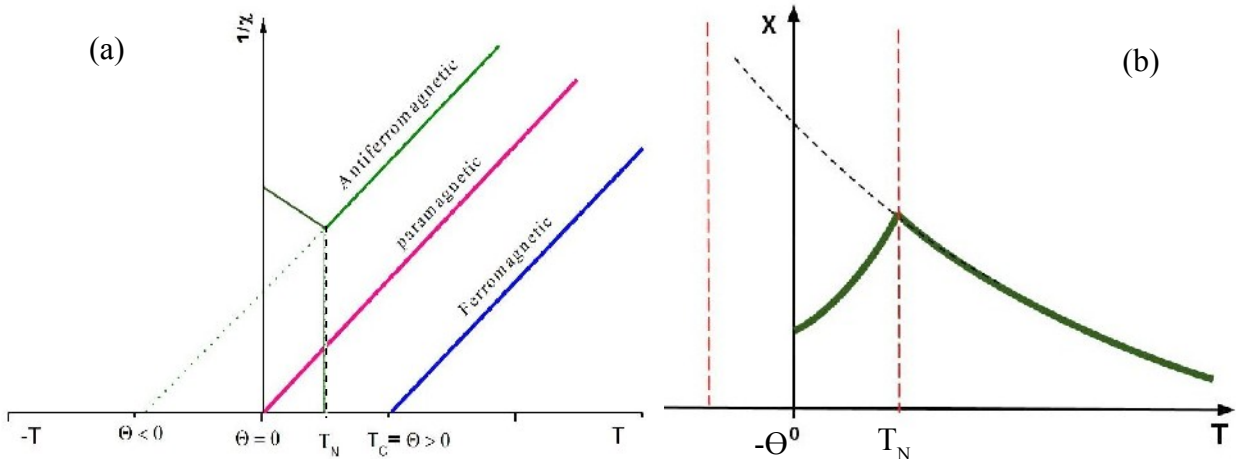

Figure 2.4 (a) Inverse susceptibility versus temperature for paramagnets ($\Theta=0$), ferromagnets ($\Theta>0$), and antiferromagnets ($\Theta<0$). (b) Temperature dependence of magnetic susceptibility for antiferromagnet, showing transition from paramagnetic to antiferromagnetic at T_N [25].

2.2.2 Effective interaction in orthovanadates (RVO$_3$)

As can be seen in Fig. 2.2 and discussed in section 2.1, the decreasing of ionic radius (IR) of rare-earth ions in orthovanadates is accompanied with increasing rotation of octahedral VO$_6$ in orthorhombic perovskite structure. Therefore, the effective net change of T$_N$ is strongly dependent on the bond length and the bond angle of V-O-V in RVO$_3$ compounds. This mismatch between the bond lengths and the bond angles can induce a distortion in the system [7], causing a significant change in the Néel temperature.

The magnetic properties of the orthovanadates depend on the various ions that are located in the crystal lattice. The ions with unfilled electron shells are involved in magnetic behavior, because each unpaired spin carries a magnetic moment [2]. The transition metal ion in orthovanadates is vanadium with two unpaired electrons 3d^2 (S=1). The two unpaired spins of each vanadium ion (V^{3+}) couple with another V^{3+} ion through the chemical bonding in the lattice to form spin alignment (parallel or anti parallel) which is described by the exchange interaction. In orthovanadate compounds (RVO$_3$), the exchange coupling between metal ions (V^{3+}) can not take place directly through the electrostatic (Coulomb interaction) energy (e^2/r$_{ij}$) between electrons of V-V bonds because the ions are too far apart. However, the unpaired cation spins couple through the anion orbital (oxygen ion) state to create indirect coupling [2, 3]. This indirect coupling is called "superexchange interaction" that corresponds to virtual spin transferring (spin coupling) between V^{3+} ions through the occupied 2p orbitals of oxygen ions. The cation-anion-cation arrangements (V-O-V) in orthovanadates produce particular spin alignments that are the most important factors for magnetic properties, as shown in Fig. 2.5 [2, 25].

Figure 2.5 Geometry of the indirect interaction in RVO$_3$ metal-oxide along V-O-V bonds, adopted from Ref. [2].

For orthovanadates RVO_3, the superexchange interaction induces antiferromagnetic behavior between the spins of the two V^{3+} ions. This interaction is along the nearest neighbor ions of the octahedral VO_6 array and strongly depends on the bond angle and the bond length of V^{3+}-O^{2-}-V^{3+}. This interaction becomes effective around magnetic transition temperature (T_N). The antiferromagnetic alignment of V-O-V increases by decreasing temperature (below Néel temperature). The superexchange interaction has a largest interaction and greatest stabilization energy when the V-O-V bonds aligned perfectly antiparallel (180°) [2]. This exchange coupling is well described by the antiferromagnetic Heisenberg Hamiltonian in Eqn. 2.19 [28, 30].

$$H^{spin} = -2 \sum_{i<j} J_{ij} S_i \cdot S_j \qquad (2.19)$$

Here H^{spin} is a Hamiltonian of exchange interaction energy between the magnetic ions that is the most responsible interaction for antiferromagnetic magnetic ordering. J_{ij} is the exchange coupling constants (coefficient), J is positive for ferromagnetic and negative for antiferromagnetic interactions, which is proportional to the superexchange energy [2, 3]. For example, the V-O-V bond angle of LaVO$_3$ is about 158° and this angle decrease to 144° for YVO$_3$ [31]. The bond angle of V-O-V is changed due to the structural transition of these compounds below room temperature.

2.3 Electrical properties

Electrical properties of materials can be classified into three types: Insulators, semiconductors, and metals. The differences among all these materials are related to how the electrons are distributed in energy bands (conduction and valence bands). The valence band is filled by electrons, and the conduction band is vacant at 0 K for band insulators and semiconductors. The band gap (E_g), difference in highest energy state of the valence band and the lowest energy state of conduction band, is very large in insulators [25]. Unlike the insulators, the semiconductors have a small band gap. It is therefore possible to excite electrons from the valence band to the conduction band at finite temperatures (T). The resistivity of the semiconductors decreases by increasing temperature and is controlled by $E_g /k_B T$ factor [25]. If the crystal is very pure, the number of conduction band electrons is equal to the number of valence band holes, and it is called an intrinsic semiconductor. However, if impurities contribute to the carrier densities, it is called an extrinsic semiconductor [27]. In contrast, the band gap is zero in metals, so the electrons can travel freely. Resistivity increases by raising the temperature, because higher temperature increases the lattice vibrations (phonons) and collisions of free electrons [25].
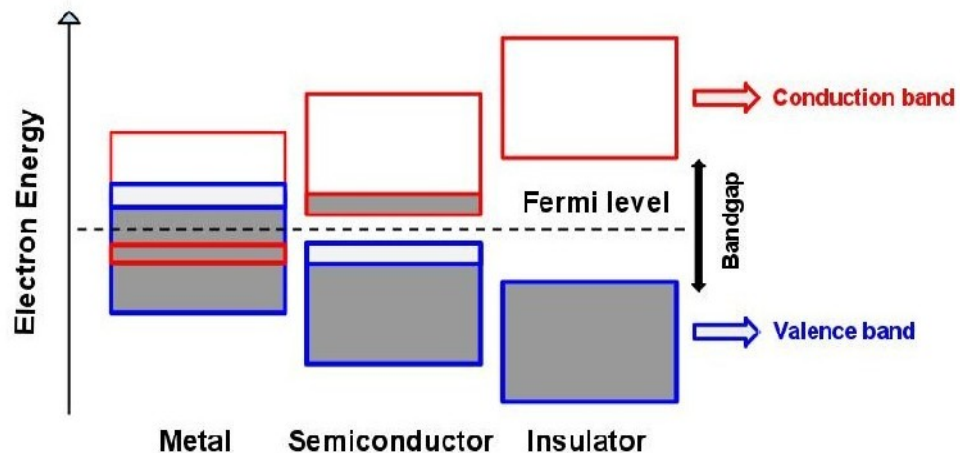

Figure 2.6 Electronic band structure of metals, semiconductors, and a typical insulators.

Another type of electronic materials are "Mott" insulators which are often found in the metal-oxides [32]. In these materials the electrons transfer between transition metal ions through the oxygen $2p$ shell [32]. In RVO_3, the metallic cations V^{3+} is surrounded by the six octahedral O^{2-} anions. The narrow bands of the unfilled $3d$ electron orbitals of V^{3+} in the VO_6 octahedral, with bandwidth of W, are not able to conduct electric current. If the electrons want to transfer between the neighboring ions of V-O-V bonds, the Coulomb repulsion energy of d-d electron correlation ($U_{dd} = < e^2/r_{12} >$), should be less than the bandwidth energy (W) [32]. But in Mott-insulators U_{dd} is greater than W, therefore the electrons are non-conducting (insulator) [33]. Also according to the Band theory of the solids, any unpaired electron in solid is free to move. Therefore, $LaVO_3$ compounds with two unpaired electrons in 3d state of the metal ions of vanadium site should have metallic behavior. But the experimental results show the insulator behavior ("Mott" insulator), this is due to higher Coulomb repulsion potential energy than bandwidth of V-O-V bonds in $LaVO_3$.

2.3.1 Temperature dependence of resistivity

Resistivity measurement for polycrystalline orthovanadate samples may give different and more complicated results than on single crystal. It is possible that the measured resistivity of these polycrystalline materials shows higher, lower or even similar resistivity compared to single crystals [34]. Also, the resistivity behavior of these compounds is strongly influenced by either the structural and the magnetic phase transition or growing them in the form of the doped orthovanadates [35]. The majority of orthovanadate compounds, with unfilled 3d bands, are semiconductors or insulators. The electrical properties of RVO_3 materials depend on the two factors, one is the charge carriers, as harbored by unpaired electrons (outer shell electrons), and another is a mechanism to enable the charge carriers to be free or activate from ionic bonds [2].

It is believed that the low mobility current carriers in the orthovanadates are small polarons. The polaron is the trapping of the electrons or holes by the local lattice polarization [27, 33]. The charge carriers are dressed in a "phonon cloud" producing a

lattice distortion of radius r_p. Polarons are "small" when $r_p \leq a$, where a is the lattice constant [36]. The small polarons are localized at lattice sites at low temperature, therefore they can not move freely and can not conduct electricity, thus showing insulating behavior [36, 37]. The localization of polarons can be broken up by increasing the temperature and lattice distortion. Therefore, the polarons can move from one site to another by thermally activated hopping process [36] and the carriers excited along bonds and increase the conductivity [27, 31, 34, 37].

The activation energy between the carriers of the t^2_{2g}—$2p\pi$—t^2_{2g} states in V-O-V bonds can be determined by using Arrhenius equation [9, 27, 37]. This dependence is described in the following equation

$$\rho = \rho_0 \, e^{\left(\frac{E_a}{k_B T}\right)}. \tag{2.20}$$

Where ρ corresponds to the resistivity of the samples at temperature T, k_B is the Boltzmann constant and E_a is the activation energy [31, 34].

Ondo *et al.* [12] reported the temperature dependence of electrical resistivity for perovskite system RVO_3. They showed that the resistivity increased with decreasing the ionic radius of R^{3+} ions in orthovanadates. Because, the decreasing of ionic radius of R^{3+} ions from La to Nd distort the symmetry of RVO_3 compounds and reduce the effect of hopping integral. Their results show that the $LaVO_3$ has higher conductivity than other orthovanadates. Also, as reported in many works [3, 4, 23, 24], the $LaVO_3$ is known as a Mott-insulator that the transition between its insulator to metallic behavior is not sharp [20]. Therefore, it is also described as a semiconductor with an activation energy and band gap of 0.12 eV and 1.1 eV, respectively [16, 35].

Chapter 3

Experimental procedures and methods

3.1 Sample preparation

High-temperature solid-state reaction is usually used for synthesizing many orthovanadates. Bulk polycrystalline $La_{1-x}Bi_xVO_3$ samples were fabricated in a two step process: First, polycrystalline samples of $La_{1-x}Bi_xVO_4$ were synthesized by a high-temperature solid-state reaction in the air. The chemical reaction is as follows:

$$\frac{(1-x)}{2}La_2O_3+\frac{1}{2}V_2O_5+\frac{x}{2}Bi_2O_3\rightarrow La_{1-x}Bi_xVO_4.$$
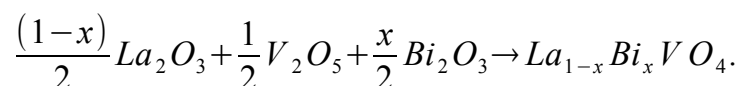
The stoichiometric amounts of La_2O_3 (99.99 wt% purity) were preheated in the furnace for three hours at 1223 K to remove any hydrated or carbonated species to form a pure powder. Appropriate proportions of V_2O_5 and Bi_2O_3 powder were added to lanthanum oxide. The mixture of powders were ground up and pressed into pellets, 15 mm in diameter and 2-4 mm in thickness, under 12 tons pressure, as illustrated in Fig. 3.1. The solid state reaction usually does not complete on the first annealing step, regrinding and reheating processes are necessary [35]. The prepared tablets were annealed in the air at 1123 K in a furnace for 3 hours. The pellets were reground, repelletized and annealed again at 1223 K for thirty (30) hours.

In a second step, the perovskites $La_{1-x}Bi_xVO_3$ samples were prepared by reduction reaction for $La_{1-x}Bi_xVO_4$ samples in a furnace at 1323 K for ten hours in flowing Argon (90%) and Hydrogen (10%) gases. This step is shown with details in Fig. 3.2. The Argon gas is usually used for diluting the Hydrogen gas through the entire system. The reduction of $La_{1-x}Bi_xVO_4$ to form $La_{1-x}Bi_xVO_3$ is shown below.

$$La_{1-x}Bi_xVO_4+H_2\rightarrow La_{1-x}Bi_xVO_3+H_2O$$
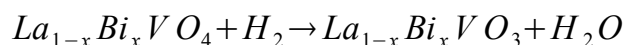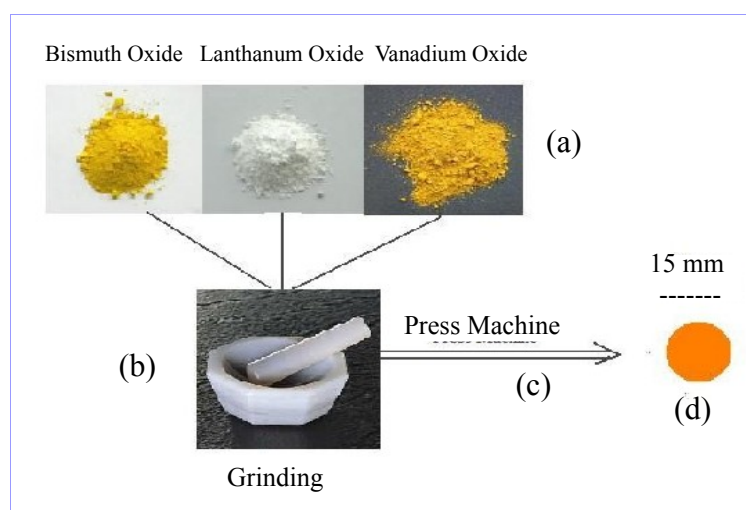
Figure 3.1 Steps of the precursor mixture, (a) the initial high purity of Bi_2O_3, La_2O_3, and V_2O_5 powders, (b) thoroughly mixing, using mortar and pestle to obtain homogeneous mixtures, (c) hydrostatic pressure under 12 tons, and (d) tablet form of the samples by 15 mm in diameter.
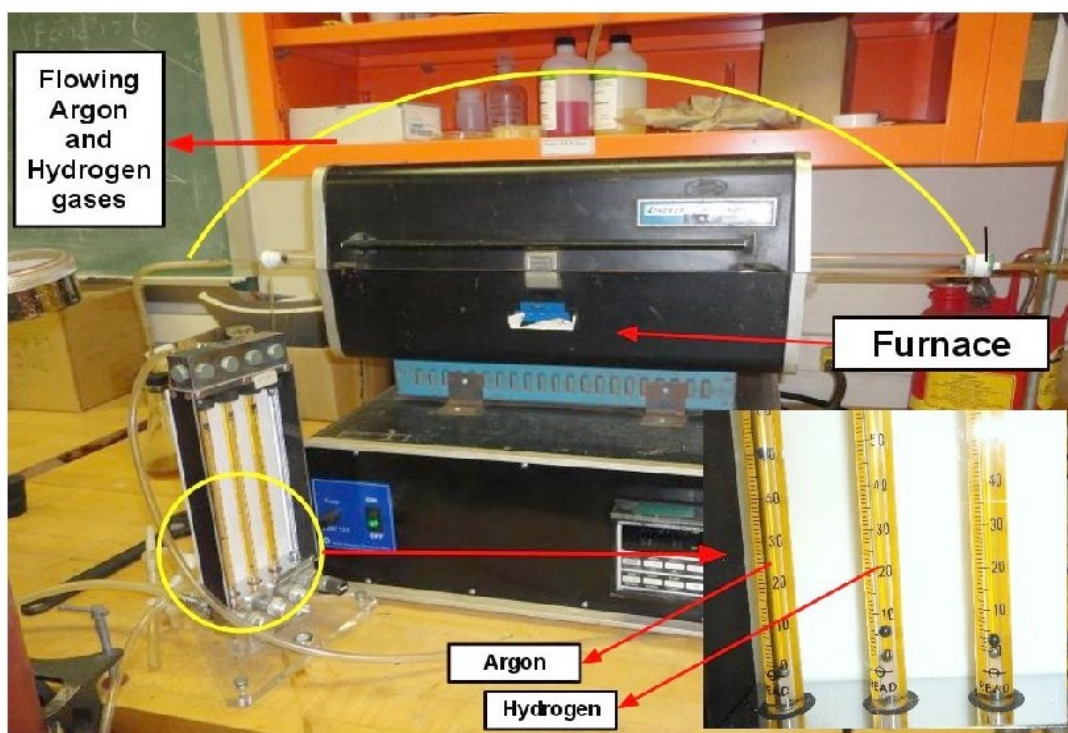
Figure 3.2 Set up for reduction of $La_{1-x}Bi_xVO_4$ to $La_{1-x}Bi_xVO_3$. This was achieved by sintering the samples in a reducing ambient, namely 90% Ar + 10% H_2. The sample was placed inside a quartz tube; flow-meters were used to ensure gas ratio, as shown at inset.

Compositional and structural properties of the prepared products were obtained via two techniques. First, energy-dispersive analysis of x-ray (EDAX) method was used to monitor the exact elemental compositions of each sample. Second, x-ray diffraction (XRD) was used to determine the crystal symmetry and the crystal structure of the samples. Also, the magnetic and the electrical properties of the samples were measured by using the magnetic property measurement system (MPMS) and the physical property measurement system (PPMS), respectively.

3.2 Energy dispersive analysis of x-rays (EDAX)

Bombardment of any unknown sample with an electron beam generates many emitted x-rays. The penetration depth of the electron beam depends on the electron beam energy and density of the sample. The interaction volume extends to the highest penetration depth, as shown in Fig. 3.3 (b). Among these emitted rays, characteristic x-rays are used to identify the elemental composition of the unknown samples. The principles of the EDAX technique are based on analyzing the properties of the characteristic x-rays [34]. The energy of the incident electron beam should generate enough energy to excite an electron of an atom from the inner-shell (K-shell) in a specimen. Electron transitions from the outer-shell to the inner-shell result in x-ray emission as shown in Fig. 3.4 (a). As indicated in this Figure, the transition from L-shell to K-shell is called K_α x-ray and from M-shell to K-shell produces K_β x-ray. K_α beams have a higher intensity than K_β beams. Each of these x-rays offers a unique signature for each atom that is present in the sample [34], as shown in Fig. 3.4 (b).

The emitted x-rays are collected by a detector, which is usually made from a high-quality doped Si single crystal. The detector is able to sort all collected x-rays by separating them into the energy spectrum from energy range of 1-20 keV. The Si single crystal is doped with lithium. The lithium is used to create a large and uniform carrier concentration through the crystal [34]. The scattered x-rays interact with the silicon atoms and excite the electrons from the valence band. Therefore, the crystal generates an electrical charge and becomes conductive while the detector electronics convert the energy of individual absorbed x-ray into the output voltage [38, 39, 40].
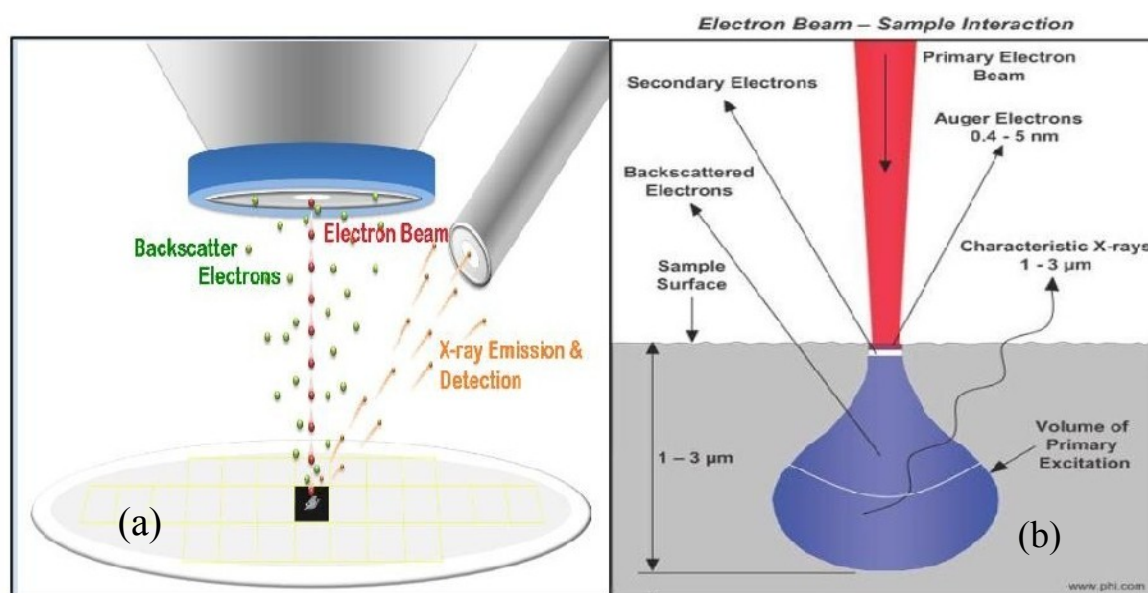
Figure 3.3 (a) EDAX measurement that electron beam incident to the sample and emitted x-ray count by detector and (b) Interaction or analysis volume is generated by bombardment of a sample by an electron beam (www.phi.com).
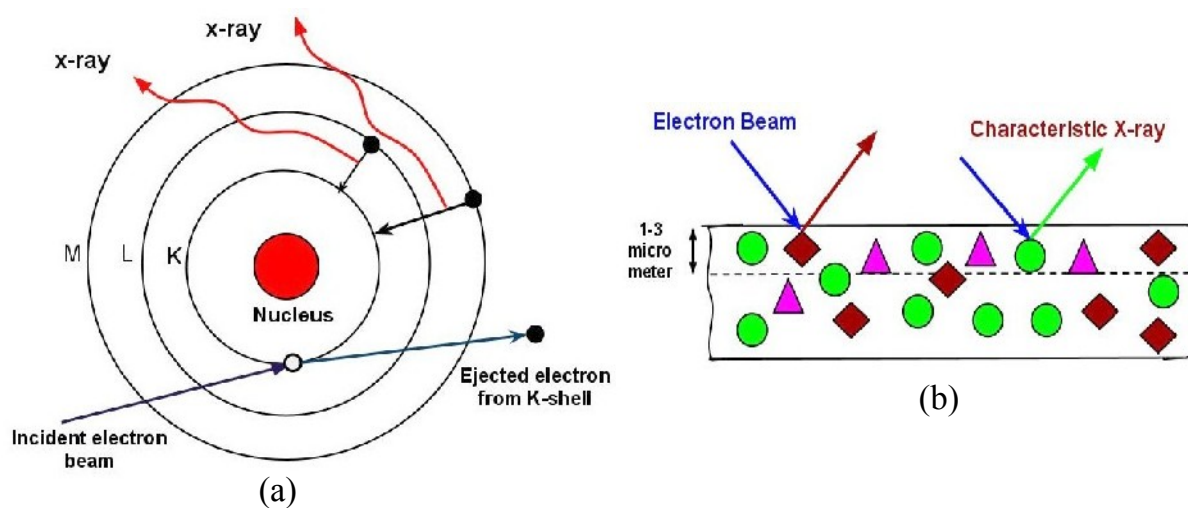
Figure 3.4 (a) Interaction of the electron beam with the K-shell electron and emission of characteristic x-ray by falling electron from outer to inner shell and (b) interaction of the electron beam with each atom in a sample produces the characteristic x-rays.

3.3   X-ray diffraction (XRD)

X-ray diffraction is an important method for characterization of materials in order to identify the crystal structure and crystal symmetry. The peaks in the x-ray diffraction patterns are related to atomic interplane distance in the crystal lattice and explained by Bragg's Law.

$$2\,d_{hkl} \cdot \sin\theta = n\,\lambda \tag{3.1}$$

In Eqn. 3.1 λ is the wavelength of the x-ray, θ is the Bragg angle between the incident beam and the crystal plane, n is the integer representing the order of diffraction, d_{hkl} is the inter-planar spacing. The Bragg condition is valid when $\lambda \leq 2d$. For a system with orthorhombic symmetry, the d-space factor can be calculated by using Eqn. 3.2 [41].

$$\frac{1}{d_{hkl}^{\,2}} = \frac{h^2}{a^2} + \frac{k^2}{b^2} + \frac{l^2}{c^2} \tag{3.2}$$

Where a, b, and c are lattice parameters. h, k, and l values are the indices of the planes as shown in Fig. 3.5.

The x-ray source is usually a particular metal target, for example Cu, located in the x-ray tube. The x-ray tube is shown in Fig. 3.6 (a). The electron beam is generated at the cathode by a filament. The electrons bombard the Cu-target (anode) and produces different emitted radiations. The mixture of characteristic x-ray and continuous x-rays travels out the tube windows. There are several ways to make monochromatic x-rays. One is to use Ni filter at the tube windows for the Cu-target. By choosing Ni, only the desired Cu radiation, usually K_{α}, is collected by the detector [34, 42]. Constructive interference creates a scattering when Bragg's Law is satisfied. The scattered x-rays are counted by the detector. The detector is able to sort all collected x-rays by separating them to the different Bragg angles (2θ) [34]. The diffracted x-rays are detected by a photon counter. The counter has the ability to measure the energy of individual x-ray photons. A typical x-ray system is shown in Fig. 3.6. The detector and sample are rotating to capture all diffracted beams.
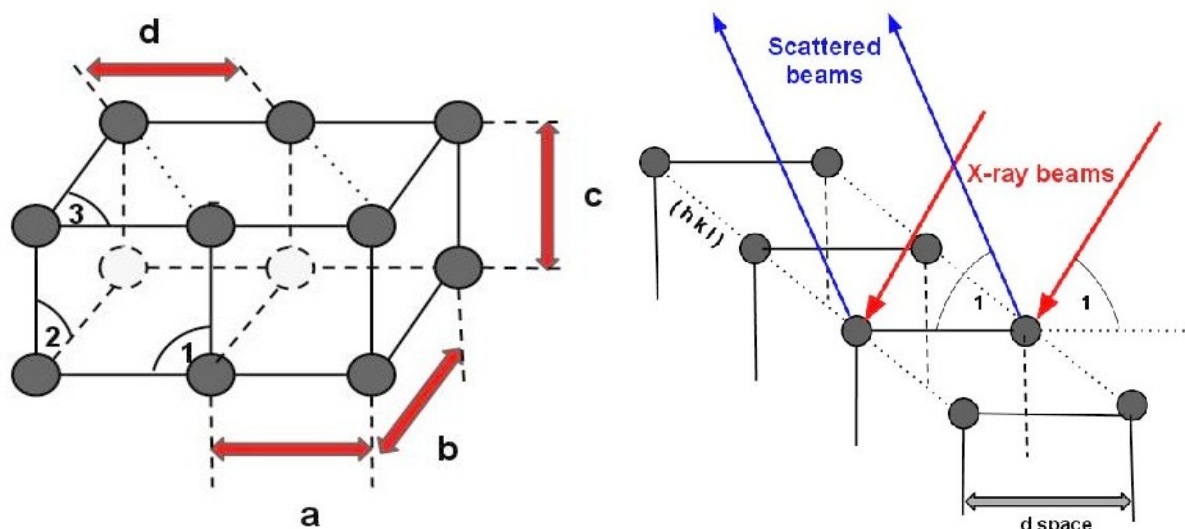
Figure 3.5 Cell parameters and d-space are shown for an unit cell (left side). The incident x-ray beam scattered from each atom which indicates Bragg's Law (right side). Angle marked "1" is the θ of Equation 3.1.
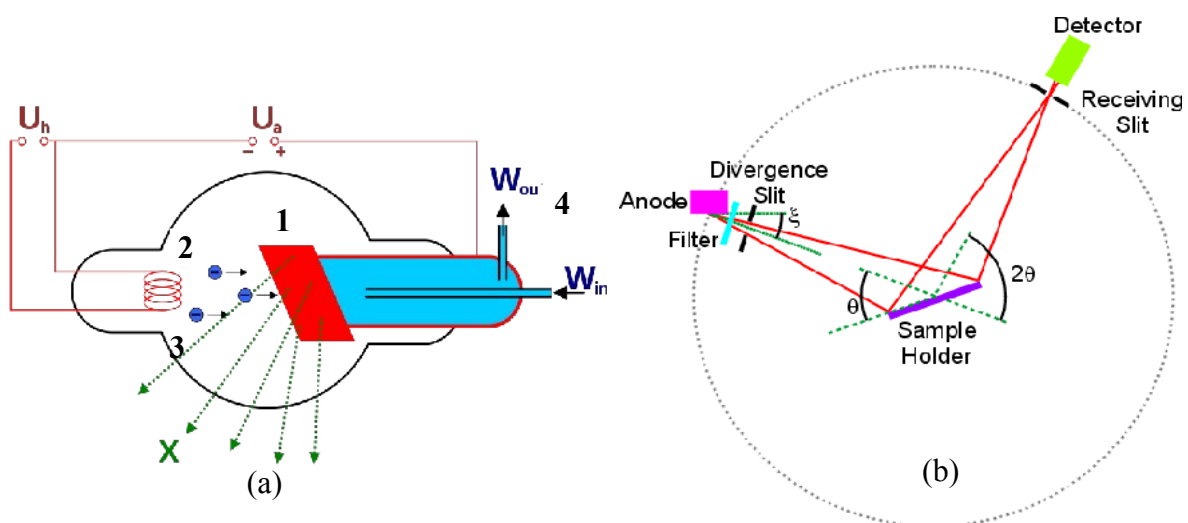
Figure 3.6 (a) X-ray tube, showing (1) anode (Cu-target), (2) filament that generates an electron beam (cathode), (3) tube window, and (4) cooling water to protect the tube from over heating [www.chemwiki.com]. (b) A typical detector configuration, the anode is fixed, the sample and detector are rotating by θ and 2θ, respectively [http://pd.chem.ucl.ac.uk/pdnn/inst1/optics1.htm].

3.4 Magnetic property measurement system (MPMS)

The MPMS is widely used in research and technology for exact measurements of the magnetic properties of materials. Superconductivity is the most important property of all the components of MPMS that enable the system to have highest sensitivity to detect a weak magnetic moment of a sample in a temperature range or applied magnetic field [29]. The SQUID device is shown in Fig. 3.7. This device is connected to two sets of detection coils. The Pickup coil and Input coil induce external flux into the SQUID [29] while SQUID electronics convert the magnetic flux to a voltage signal at the output of the SQUID [43, 44, 45, 46]. The dependence of the output voltage to the sample position is shown in Fig. 3.7 (7).

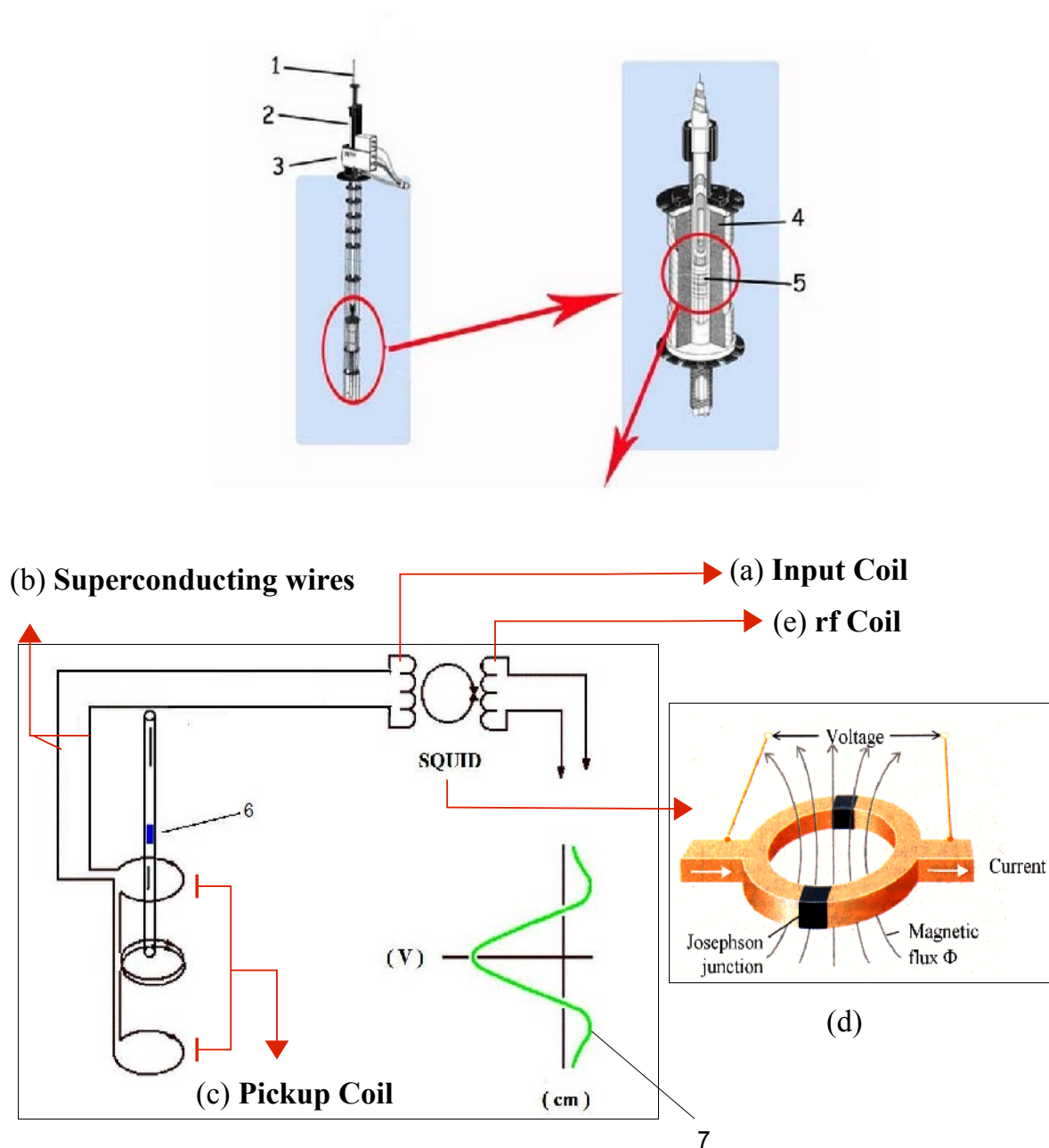Figure 3.7 Magnetic property measurement system set up, (1) sample rod, (2) sample transport, (3) airlock, (4) superconducting magnet, (5) detection coils, (6) sample, and (7) output voltage. (a), (b), (c), and (d) are indicated the superconducting components of MPMS.

3.5 Physical properties measurement system (PPMS)

The PPMS is a multifunctional system in order to study the physical properties of materials. The PPMS is an advanced design instrument with the ability to measure resistivity, specific heat, thermal transport and AC/DC electrotransport. One of these applications used in this project is temperature dependence of resistivity measurement. The principles of this measurement are based on the four-probe technique. As shown in Fig. 3.8, there are four wires that are pinned on the surface of the sample [34]. A current is passed between the two outer wires and voltage is measured across two inner wires. By using this method "the errors due to current crowding near a wafer edge and to pin wobble can be minimized" [47]. The voltmeter in this measurement has a very high impedance that minimizes the drop in voltage amplitude across the applied current. The exactness of this technique helps to measure a very small voltage and a current drop during cooling or heating of the sample [34].

The DC resistivity is calculated by using Ohm's Law where resistivity is defined as:

$$\rho = R \cdot \left(\frac{A}{L}\right) \tag{3.3}$$

Here R is resistance, A is cross-section area of the sample, and L is the distance of the inner wires that are connected to the voltmeter. The sample holder (puck) has three bridges, each of which provides four independent channels (four-probe resistance measurements) as shown in Fig. 3.8. This design enables PPMS to make measurements of up to three samples simultaneously. All of these measurements are performed in the dewar shown in the Fig. 3.9 (a), which contains a superconducting magnet immersed in liquid helium. The inside photographic view of PPMS is indicated in Fig. 3.9 (b). The rest of the system is the computer equipment which is used for controlling the experiments.
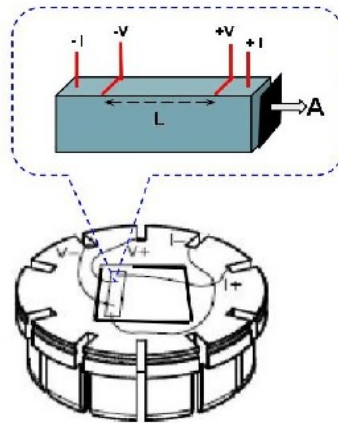
Figure 3.8 Sample in a rod form which is placed on a puck with four connections, L is the distance between two inner probes and A is the cross-section area of the rod.
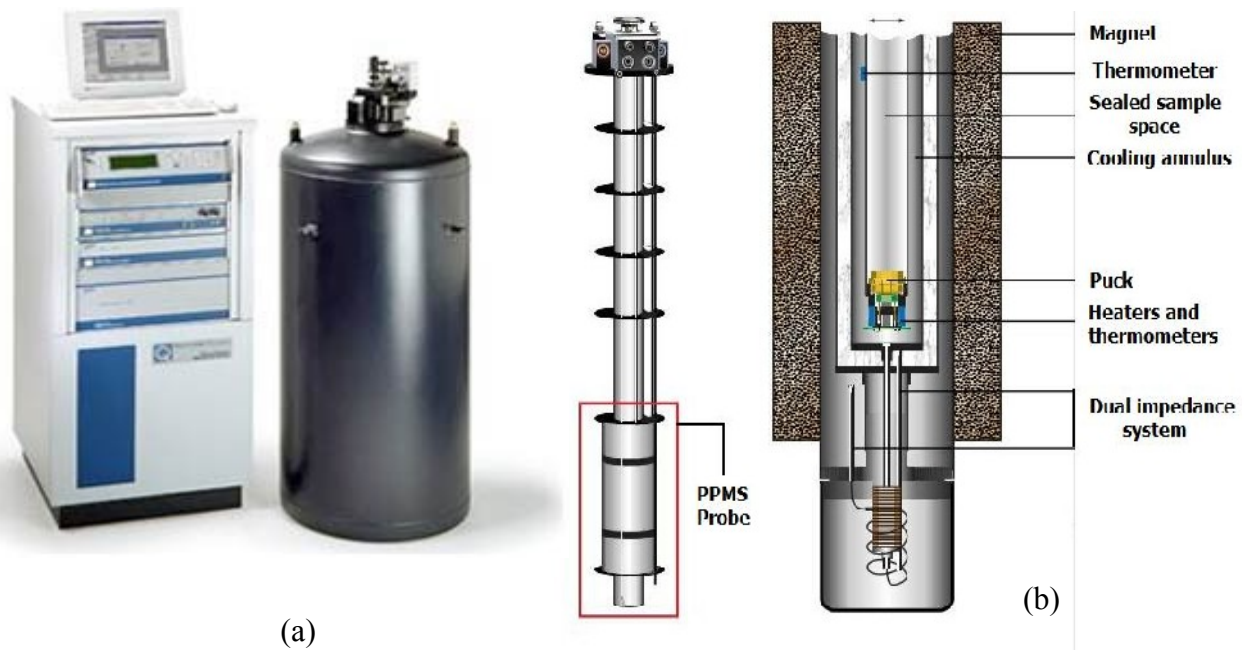

Figure 3.9 (a) Physical property measurement system [48] and (b) internal schematic of dewar in the physical property measurement system [48]. The details of the set up are indicated in the image.

Chapter 4

Results & discussions

The elemental composition of prepared samples are analyzed by EDAX technique as discussed in section 3.1. The surface images of all prepared samples are shown in Fig. 4.3. EDAX were taken at the three points of the surface of each specimen. The three scanned points are to examine the homogeneity or inhomogeneity of each sample. The results are reported as the atomic percentage with exact amount of the composition for each sample, as given in Table 4.1. The measured oxygen concentration for all samples, as give in Table 4.1, have a large error. The goal is to determine whether or not the percentage of La,V and Bi elements in $La_{1-x}Bi_xVO_3$ compounds is in agreement with those obtained by stoichiometry analysis [49, 50]. The EDAX spectra are plotted for x-ray intensity versus electron beam energy, as shown in Fig. 4.4.

As illustrated in Fig. 4.3 and Table 4.1, for the samples where x=0, 0.04, and 0.07, bismuth was successfully doped in the La site. However, no Bi was found for the samples prepared with x > 0.1. This may be due to the low melting temperature of Bi_2O_3 and its high volatility. Thus, bismuth melted and most likely evaporated. Higher percentage of Bi in the sample might be possible through the lower annealing temperature, various annealing time, or alternative synthesis methods. High Bi content has been achieved in the synthesis of $BiMnO_3$ [51] or $BiCoO_3$ [52] using high pressure, sol gel, Pechini method synthesis routes, etc. Our detailed structural and properties analysis exhibit that for x < 0.1 we have the doped samples, whereas above x > 0.1 there is a higher amount of vanadium present which indicates the presence of a second phase.

For a prepared sample with x > 0.1, there might be a possibility of having either one of the vanadium oxide phases (VO_x) or composite phase of vanadium oxides. According to the phase diagram of Magnéli phases of VO_x that was proposed by Kachi *et al.* [53] and Kosuge [54], as given in Fig. 4.1, there are a numerous different vanadium oxide phases (single phase or composite phase) with very narrow boundary conditions between each phase. The actual phase of the segregated samples was determined by using x-ray diffraction analysis. The phase stability diagram of all samples is shown in

Fig. 4.2. The percentage of each phase in bi-phasic samples are calculated in Table 4.1.
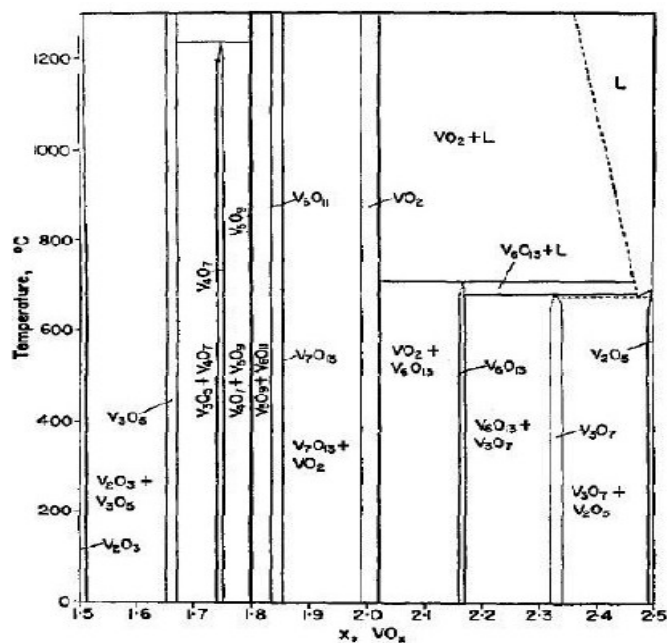
Figure 4.1 Phase diagram of Magnéli phases of VO_x, horizontal axis shows x content of VO_x phases and vertical axis indicates the temperature, adopted from Ref. [53, 54].
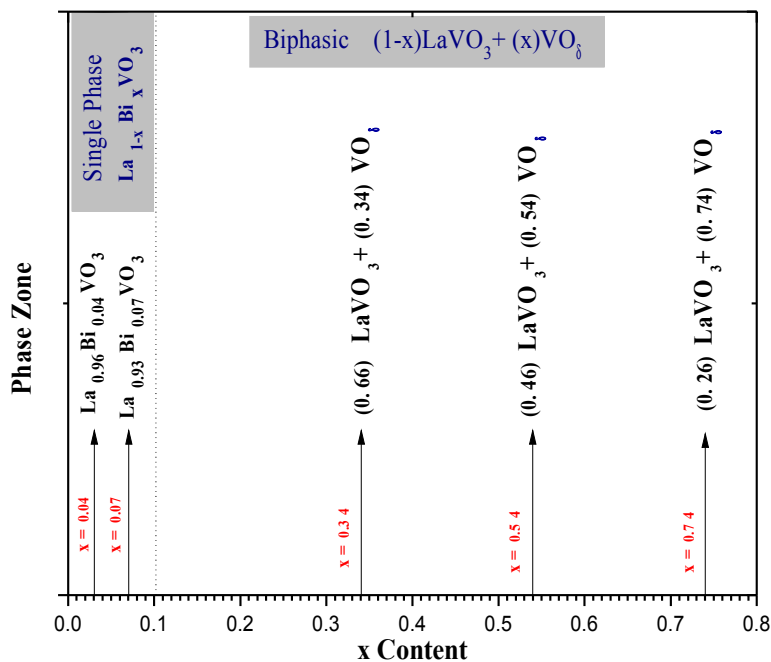
Figure 4.2 Phase stability diagram of prepared samples under the synthesis condition used in this work.
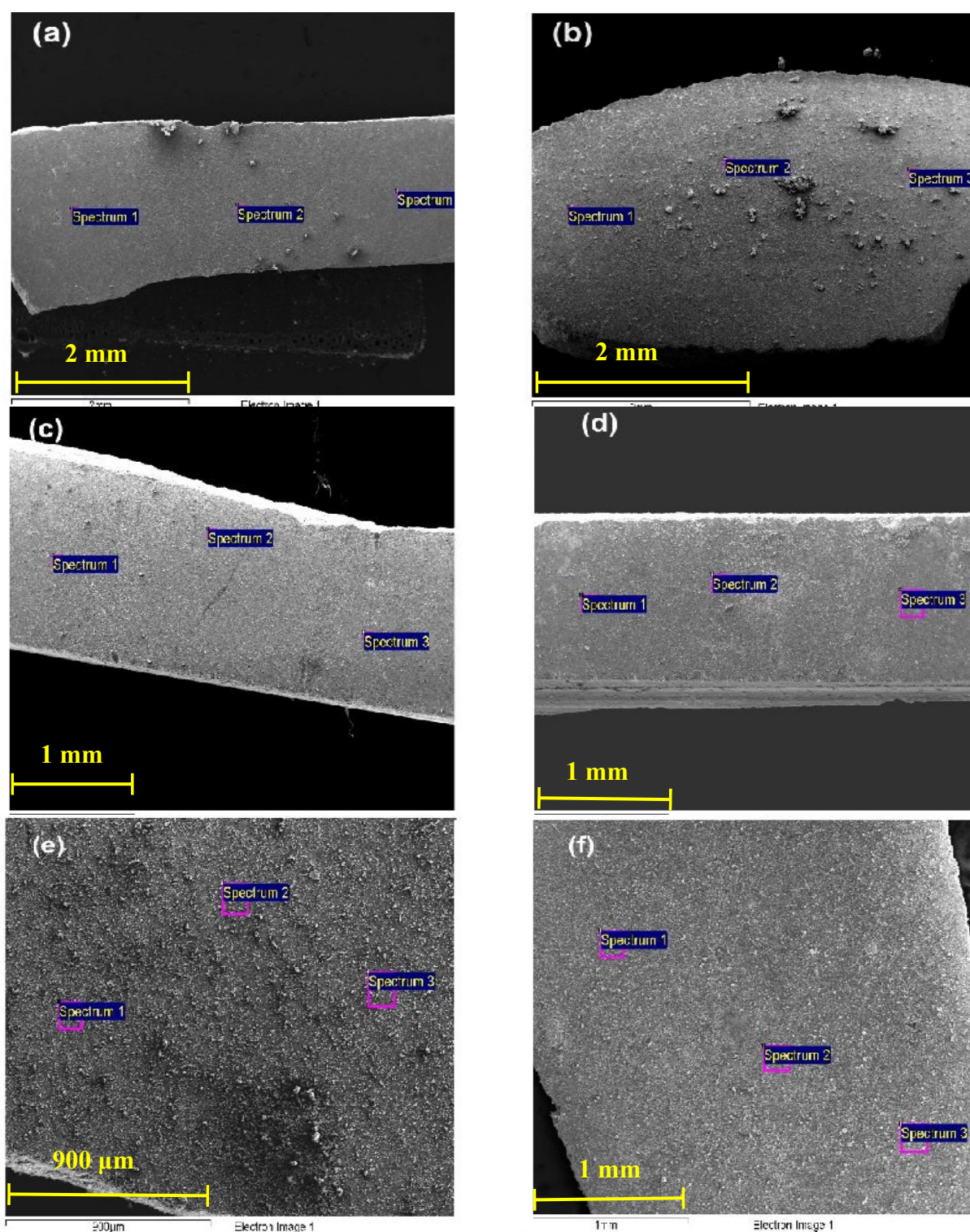
Figure 4.3 The surface image of the samples at different scales. The measurements were taken at the different points to ensure the chemical homogeneity or inhomogeneity of (a) $LaVO_3$, (b) $La_{0.96}Bi_{0.04}VO_3$, (c) $La_{0.96}Bi_{0.04}VO_3$, and (d), (e), (f) bi-phasic samples.
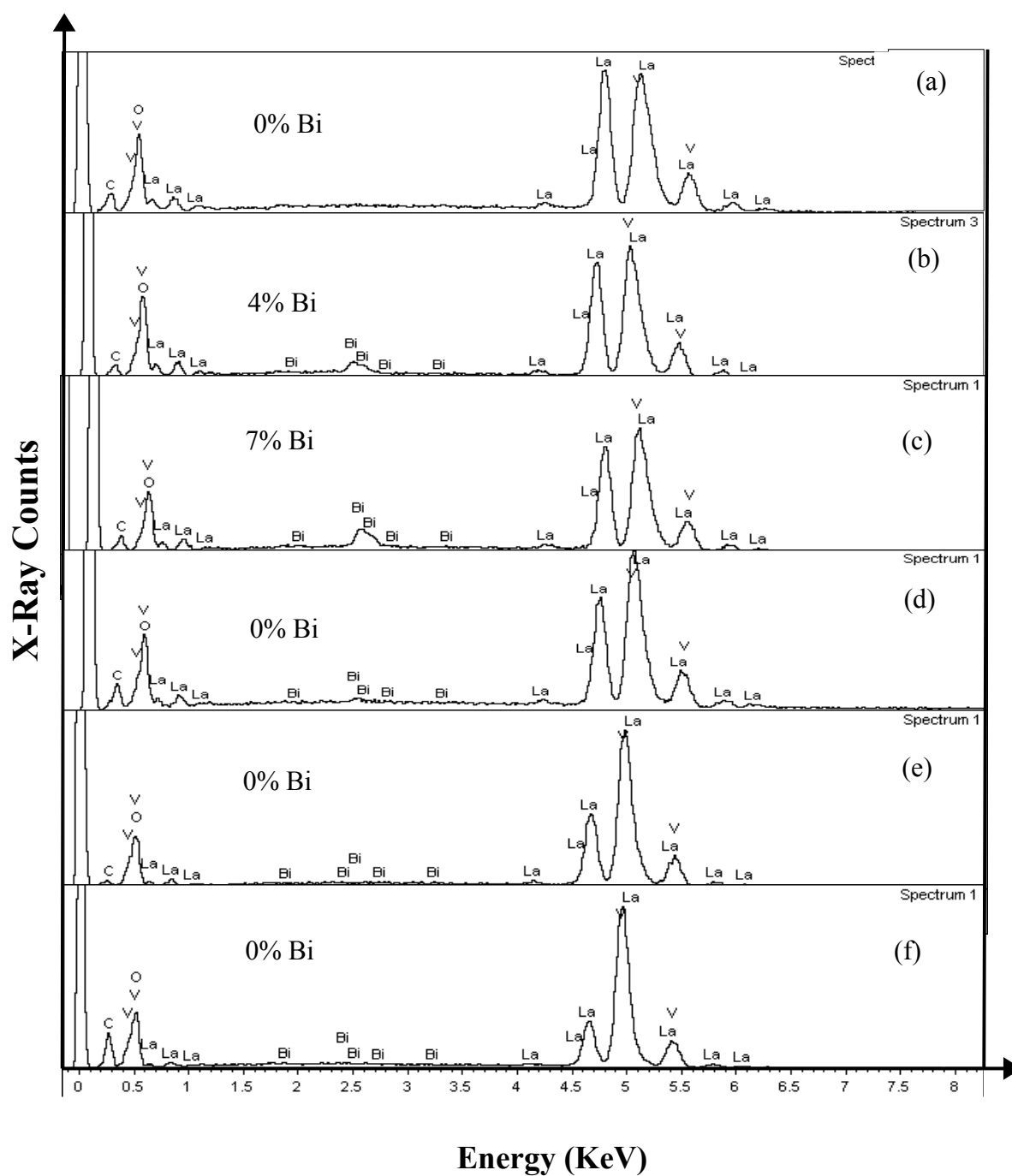
Figure 4.4 Intensity of x-ray counts versus incident electron beam energy (EDAX spectra) of (a) $LaVO_3$, (b) $La_{0.96}Bi_{0.04}VO_3$, (c) $La_{0.96}Bi_{0.04}VO_3$, and (d), (e), (f) bi-phasic samples.

Expected (a)		60.00	20.00	20.00		40
Spectrum	In stats.	O	V	La		La+V
Spectrum 1	Yes	55.90	21.42	22.68		
Spectrum 2	Yes	54.70	22.16	23.14		
Spectrum 3	Yes	55.27	22.01	22.72		
Mean		55.29	21.86	22.85		44.71
Max.		55.90	22.16	23.14		
Min.		54.70	21.42	22.68		

$$\frac{22.85}{44.71} = \frac{?(La)}{100} \quad \textbf{La} \approx \textbf{50\%}$$

$$\frac{21.86}{44.71} = \frac{?(V)}{100} \quad \textbf{V} \approx \textbf{50\%}$$

1. LaVO$_3$

| Expected (b)		60.00	20.00	19.00	1.00	20
Spectrum	In stats.	O	V	La	Bi	La+Bi
Spectrum 1	Yes	58.62	21.43	19.20	0.75	
Spectrum 2	Yes	59.21	21.26	18.80	0.73	
Spectrum 3	Yes	58.61	21.46	19.18	0.74	
Mean		58.81	21.38	19.06	0.74	19.8
Max.		59.21	21.46	19.20	0.75	
Min.		58.61	21.26	18.80	0.73	

$$\frac{19.06}{19.8} = \frac{?(La)}{100} \quad \textbf{La} \approx \textbf{96\%}$$

$$\frac{0.74}{19.8} = \frac{?(Bi)}{100} \quad \textbf{Bi} \approx \textbf{4\%}$$
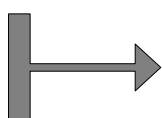
2. La$_{0.96}$Bi$_{0.04}$VO$_3$

Expected (c)		60.00	20.00	18.00	2.00	20
Spectrum	In stats.	O	V	La	Bi	La+Bi
Spectrum 1	Yes	54.24	24.23	20.14	1.39	
Spectrum 2	Yes	51.88	25.02	21.42	1.68	
Spectrum 3	Yes	53.35	24.50	20.69	1.46	
Mean		53.16	24.58	20.75	1.51	22.26
Max.		54.24	25.02	21.42	1.68	
Min.		51.88	24.23	20.14	1.39	

$$\frac{20.75}{22.26} = \frac{?(La)}{100} \quad \textbf{La} \approx \textbf{93\%}$$

$$\frac{1.51}{22.26} = \frac{?(Bi)}{100} \quad \textbf{Bi} \approx \textbf{7\%}$$
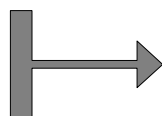
3. La$_{0.93}$Bi$_{0.07}$VO$_3$

	LaVO₃				VOₓ
	LaVO₃				**VOₓ**
Expected	60.00	20.00	0.00	20.00	40.00
Spectrum	In stat.	O	V (Total)	La	Bi	V belong to LaVO₃ phase	V belong to VOₓ phase

Spectrum	In stat.	O	V (Total)	La	Bi	V belong to LaVO₃ phase	V belong to VOₓ phase
Spectrum 1	Yes	54.33	27.24	18.21	0.23		
Spectrum 2	Yes	52.86	28.43	18.71	0.00		
Spectrum 3	Yes	56.07	26.65	17.28	0.00		
Mean		54.42	27.44	18.07	0.08	18.07	9.37
Max.		56.07	28.43	18.71	0.23		
Min.		52.86	26.65	17.28	0.00		

$$\frac{18.07}{27.44} = \frac{?V}{100}$$

66% V belong to LaVO₃

$$\frac{9.37}{27.44} = \frac{?V}{100}$$

34% V belong to VOₓ

4. [66%] LaVO₃ + [34%] VOₓ

	LaVO₃				VOₓ
Expected	60.00	20.00	0.00	20.00	40.00

Spectrum	In stat.	O	V (Total)	La	Bi	V belong to LaVO₃ phase	V belong to VOₓ phase
Spectrum 1	Yes	50.76	34.26	14.98	0.00		
Spectrum 2	Yes	50.43	34.03	15.53	0.00		
Spectrum 3	Yes	47.72	35.48	16.79	0.00		
Mean		49.64	34.59	15.77	0.00	15.77	18.82
Max.		50.76	35.48	16.79	0.00		
Min.		47.72	34.03	14.98	0.00		

$$\frac{15.77}{34.59} = \frac{?V}{100}$$

46% V belong to LaVO₃

$$\frac{18.82}{34.59} = \frac{?V}{100}$$

54% V belong to VOₓ

5. [46%] LaVO₃ + [54%] VOₓ

						LaVO₃	**VOₓ**
Expected		60.00		20.00	0.00	20.00	40.00
Spectrum	**In stat.**	**O**	**V (Total)**	**La**	**Bi**	**V belong to LaVO₃ phase**	**V belong to VOₓ phase**
Spectrum 1	Yes	58.10	33.22	8.68	0.00		
Spectrum 2	Yes	59.29	32.56	8.15	0.00		
Spectrum 3	Yes	55.12	35.60	9.28	0.00		
Mean		57.50	33.79	8.70	0.00	8.70	25.09
Max.		59.29	35.60	9.28	0.00		
Min.		55.12	32.56	8.15	0.00		

$$\frac{8.70}{33.79} = \frac{?V}{100} \qquad \textbf{26\%} \text{ V belong to LaVO}_3$$

$$\frac{25.09}{33.79} = \frac{?V}{100} \qquad \textbf{54\%} \text{ V belong to VO}_x$$
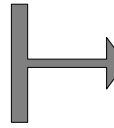
6. [26%] LaVO₃ + [74%] VOₓ

Table 4.1 Elemental composition of the prepared samples, showing the different atomic ratios of La, Bi,V, and O.

The x-ray diffraction measurement was carried out to study the crystal structure and crystal symmetry of the samples. The measurement was performed at room temperature for CuK_α radiation (λ= 1.54056 Å). The scattered x-rays were counted at angle range of 2Θ =20° to 80°. The generator voltage and the tube current were set at 32 V and 23 mA, respectively. All the measured x-ray patterns were compared with international standard database data of $LaVO_3$ and VO_x phases. In Fig. 4.5, the database data is shown for $LaVO_3$. The database data of V_2O_3 is also illustrated in Fig. 4.6. Miller indices (*hkl* values) corresponding to the each peak can be determined by comparing the diffraction patterns of all samples to the standard database data of $LaVO_3$ and VO_x phases. The lattice parameters were calculated by CrystalSleuth program to determine the crystal structure. The lattice parameters of the doped and the bi-phasic samples are given in Table 4.2 and Table 4.3.

The diffracted beams of the prepared $LaVO_3$ correspond to the diffracted peaks of the database data of pure $LaVO_3$ are shown in Fig. 4.7 and Fig. 4.8. The agreement between these two graphs illustrates that we achieved a single phase pure $LaVO_3$ sample with no impurities. The lattice parameters values of $LaVO_3$ are calculated in Table 4.2. According to the database data and the t-factor which is defined as a tolerance factor, we were able to indicate the crystal symmetry of this sample. In perovskite structure (ABO_3), the possible mismatch that may lead to a non-ideal crystal structure is defined in the following equation which is called tolerance factor [55]

$$t = \frac{(R_A + R_O)}{\sqrt{2(R_B + R_O)}}.$$

(4.1)

Here, t is tolerance factor, (R_A- R_O) and (R_B-R_O) are average ionic radii between A and oxygen ions, and B and O ions, respectively. The t factor can define the crystal symmetries of perovskite oxide, t=1 corresponds to cubic symmetry, t>1 is related to hexagonal formation, and t<1 indicates the orthorhombic or tetragonal structures. When the t factor is less than one, it is accompanied by the rotation of octahedral VO_6. This rotation causes the changes of the bond angle in V-O-V from 180° to (180°-$\Delta\theta$) [9, 55]. The angular changes of the V-O-V bonds are the important reason for the different

physical behaviors of $LaVO_3$ compound. The mismatch between ionic radii of V, La, and O ions were measured at room temperature for the parent compound. The bond lengths of La-O and V-O were calculated by using of the standard table for radii of the ions [22]. The value of t was calculated to be **0.86** for $LaVO_3$. This value shows that the crystal symmetry of $LaVO_3$ should be orthorhombic or tetragonal. By comparing the measured lattice parameters ($a \neq b \neq c$), the $LaVO_3$ has to be in orthorhombic symmetry.

Diffraction patterns for $La_{1-x}Bi_xVO_3$ samples are indicated in Fig. 4.9 and Fig. 4.10. By comparing x-ray diffraction of the parent compound and $La_{1-x}Bi_xVO_3$ samples, we deduced the crystal symmetry did not change. This shows the bismuth was substituted in La site and we had made the two single phases of $La_{0.96}Bi_{0.04}VO_3$ and $La_{0.93}Bi_{0.07}VO_3$ samples. The measured lattice parameters of the doped samples shown in Table 4.2. The t factor also can be determined for $La_{1-x}Bi_xVO_3$ samples. For doped samples that the La site is partially occupied by Bi ions for x=0.04 and 0.07, the Eqn. 4.1 is modified to the following equation

$$t = \frac{((1-x)R_{La} + (x)R_{Bi}) + (R_O)}{\sqrt{2}(R_V + R_O)}.$$

(4.2)

The value of t is about **0.86** for the $La_{0.96}Bi_{0.04}VO_3$ and $La_{0.93}Bi_{0.07}VO_3$ which equal to the $LaVO_3$. According to the value of t, the crystal symmetry remains unchanged for $La_{1-x}Bi_xVO_3$ samples (orthorhombic). The lattice parameter values are given in Table 4.2, there is a slight increase in lattice parameters and volume for the doped ($La_{1-x}Bi_xVO_3$) samples in comparison to $LaVO_3$, since the atomic number of bismuth (Z=83) is greater than that of lanthanum (Z=57).

Bi-phasic samples were also characterized by x-ray technique. X-ray patterns intensity versus 2θ of these samples are shown in Fig. 4.12. Comparing three sets of x-ray patterns of bi-phasic samples indicates an increasing in intensity of some additional peaks especially at (0 1 2), (1 1 0), (3 0 0), and (1 1 6) indices by increasing concentration of vanadium oxide. All or some of these peaks can belong to the impurities or VO_x phases. The XRD international database data of some VO_x phases were compared to the x-ray patterns of bi-phasic samples as shown in Fig. 4.11(a). We found out that all

the extra diffracted beams are exactly corresponding to V_2O_3 phase (Fig. 4.11 (b)). The lattice parameter values are given in Table 4.3. The bi-phasic samples of $LaVO_3$ and V_2O_3 are presented in different ratios. Orthorhombic and hexagonal symmetries were obtained respectively for $LaVO_3$ and V_2O_3. The similarity between the lattice parameter values of the samples with the partial V_2O_3 phase to the results of McWhan *et al.* [56] for pure V_2O_3 compound proves the synthesizing of V_2O_3 phase in bi-phasic samples as given in Table 4.3.
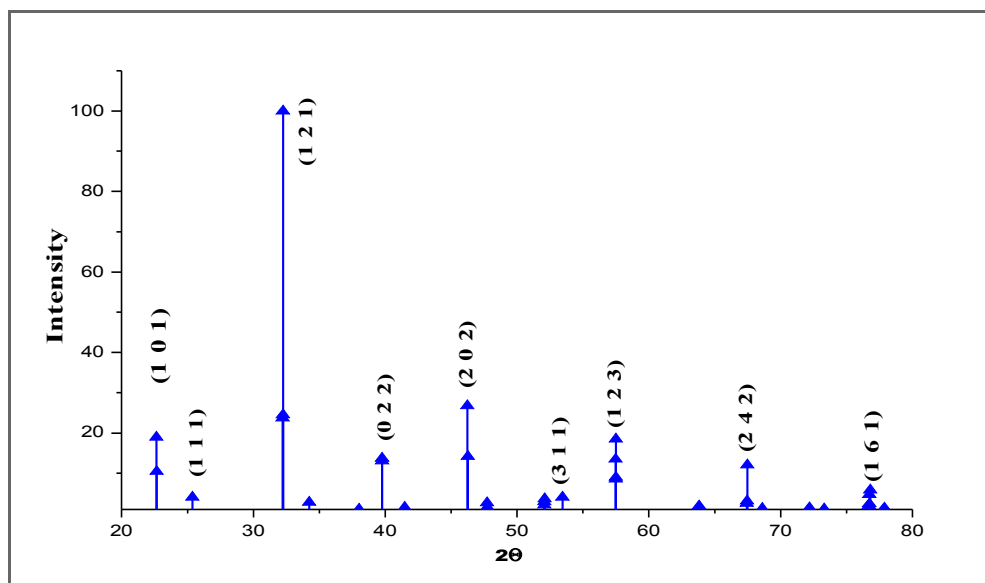

Figure 4.5 Intensity of x-rays versus Bragg angles for database data of $LaVO_3$ (JCPDS Card No: 001-6533).
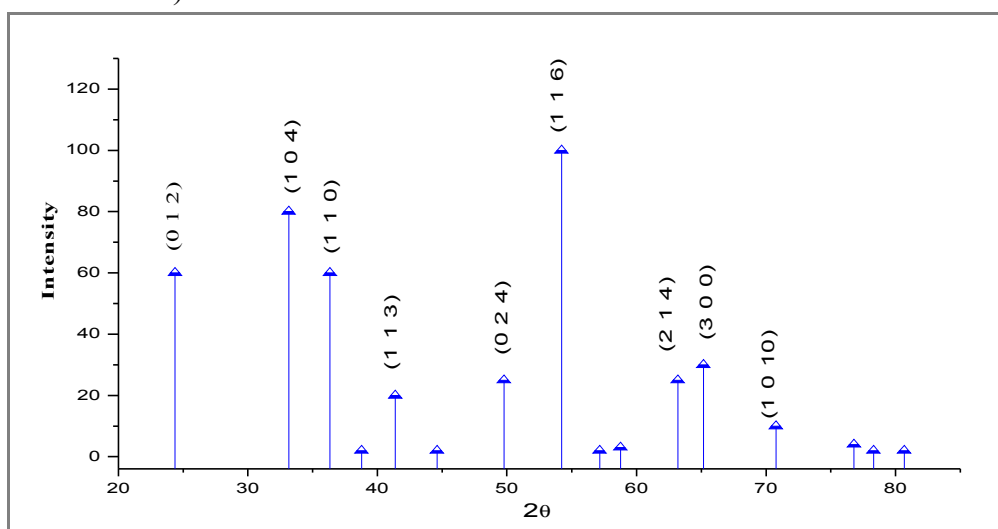

Figure 4.6 Intensity of x-rays versus Bragg angles for database data of V_2O_3 (JCPDS Card No: 001-1293).
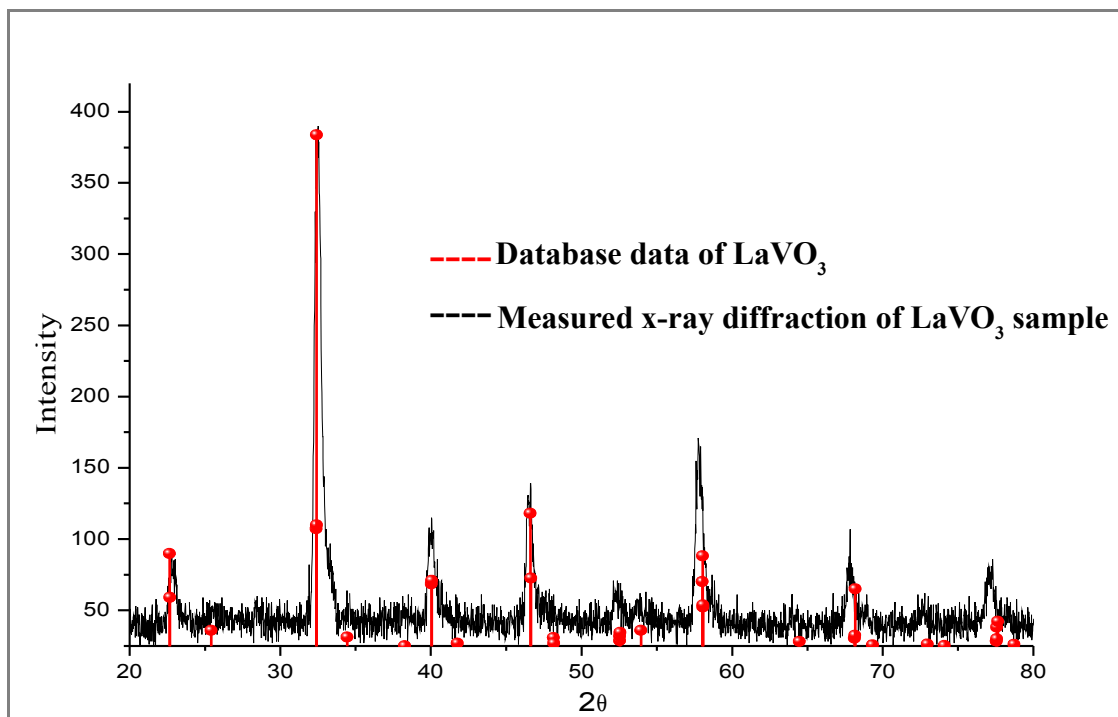
Figure 4.7 Comparison of measured x-ray diffraction pattern of LaVO$_3$ sample and standard database data of LaVO$_3$.
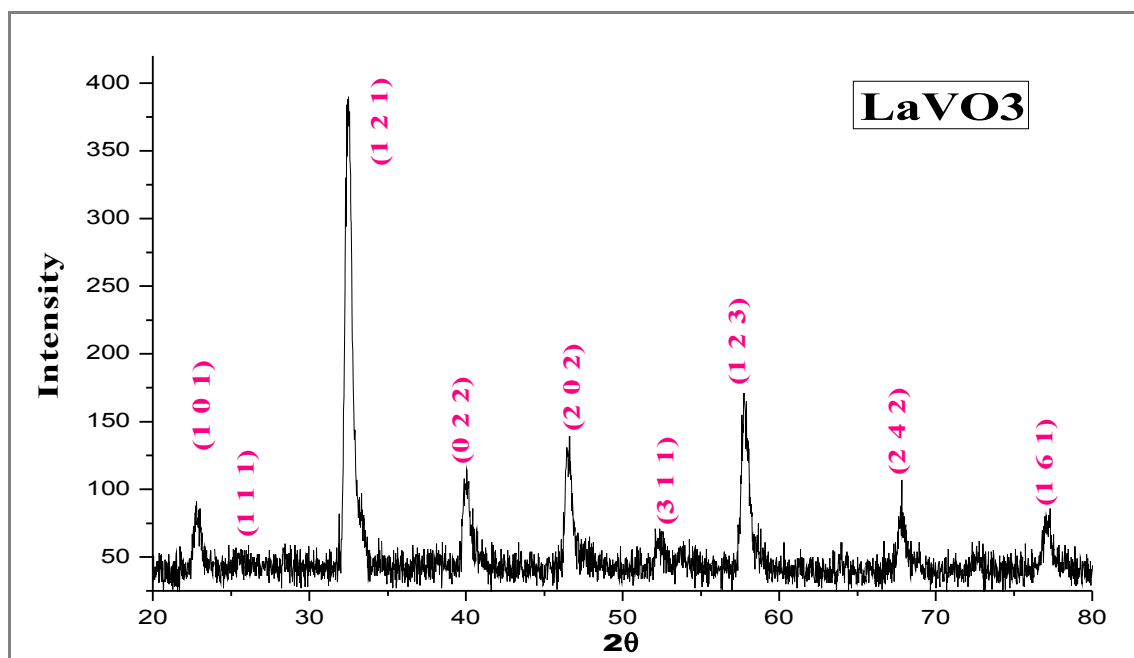

Figure 4.8 X-ray diffraction pattern of polycrystalline LaVO$_3$ sample, showing peak's positions correspond to the particular reflection indices (hkl).
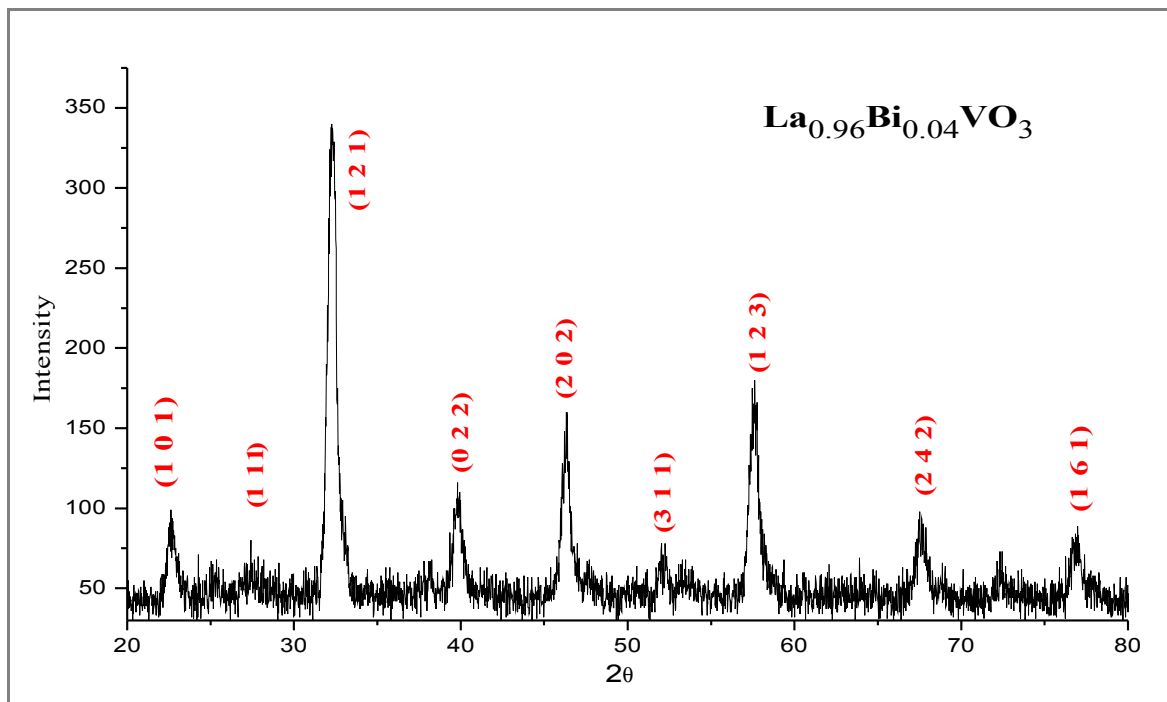
Figure 4.9 X-ray diffraction pattern of $La_{0.96}Bi_{0.04}VO_3$ sample.
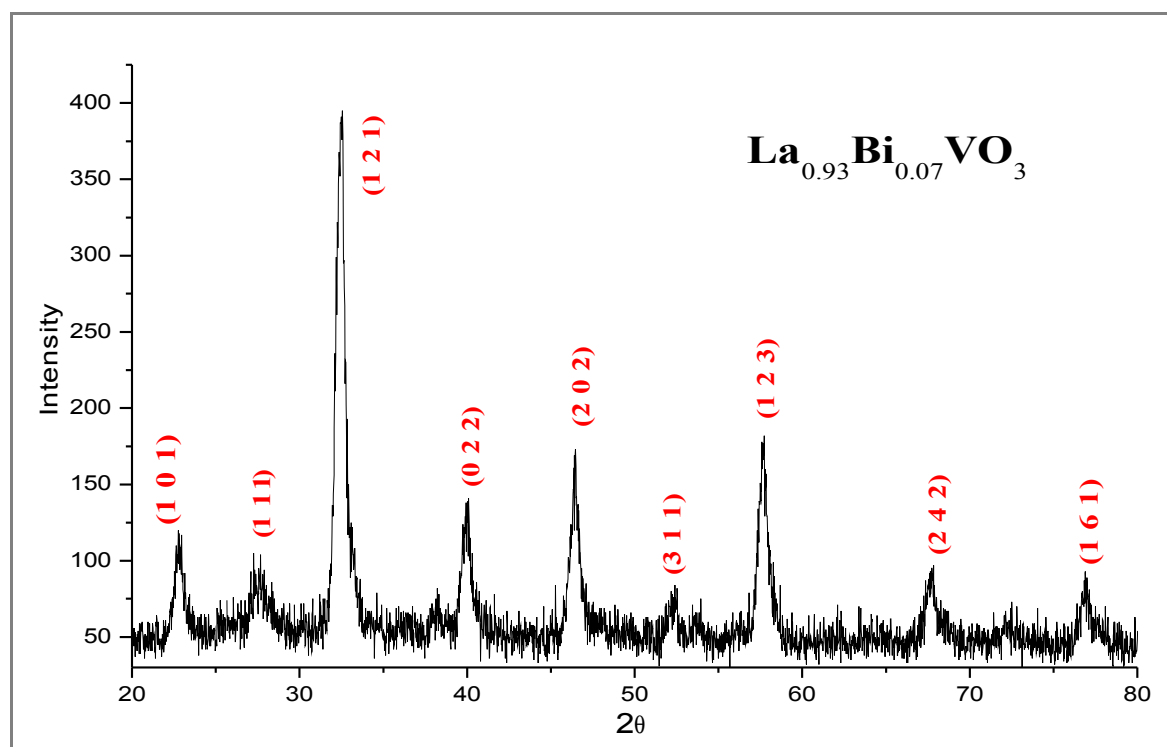
Figure 4.10 X-ray diffraction pattern of $La_{0.93}Bi_{0.07}VO_3$ sample.

Figure 4.11 (a) Comparing additional peaks in bi-phasic sample with some VO_x phases, showing all the extra peaks correspond to V_2O_3 phase and (b) comparing measured x-ray diffraction pattern of the single phase $LaVO_3$ and the bi-phasic $(x)LaVO_3+(1-x)V_2O_3$ samples.
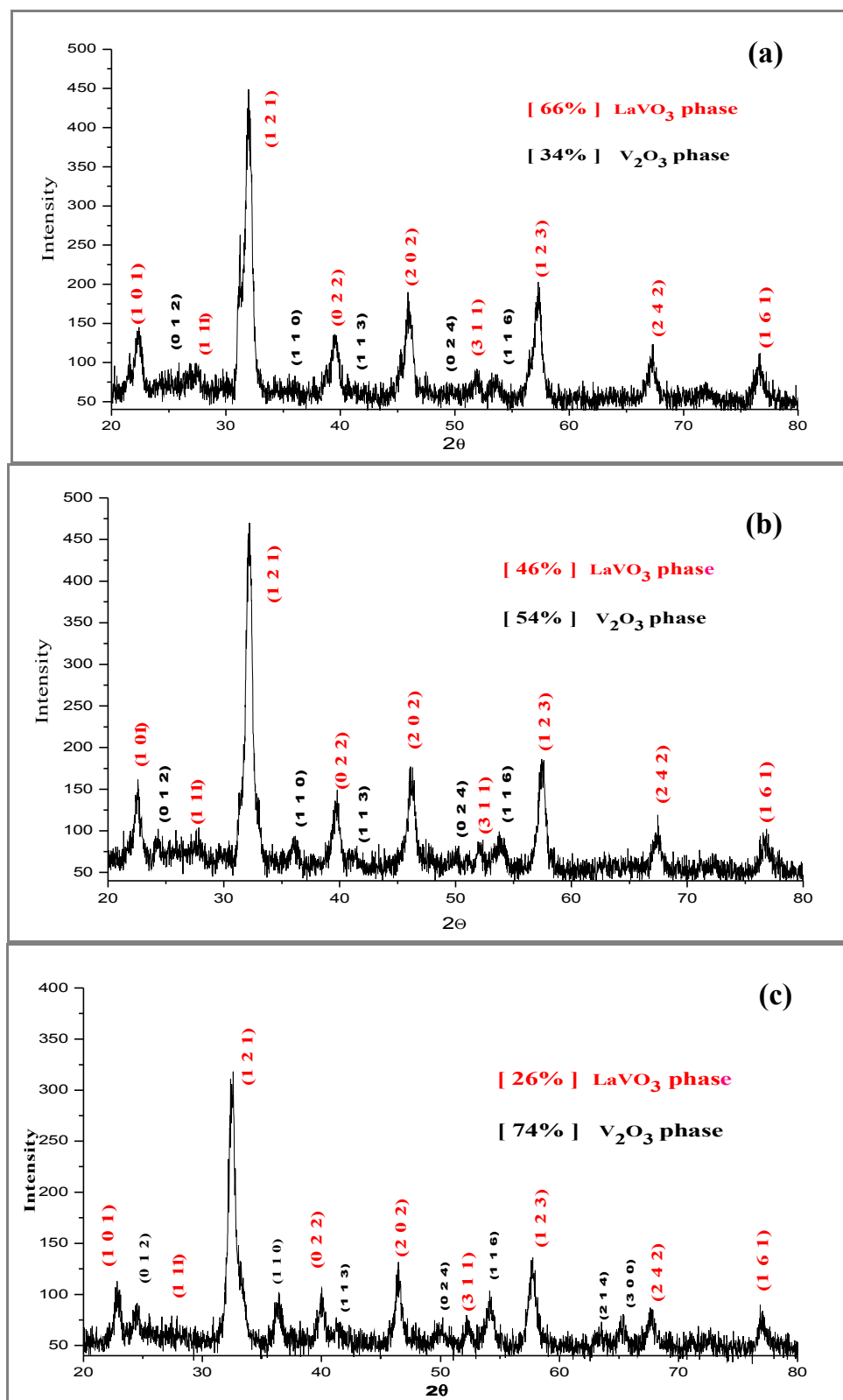
Figure 4.12 X-ray diffraction patterns of bi-phasic samples (x)LaVO₃ + (1-x)V₂O₃, (a) x=0.66, (b) x=0.46, and (c) x=0.26.

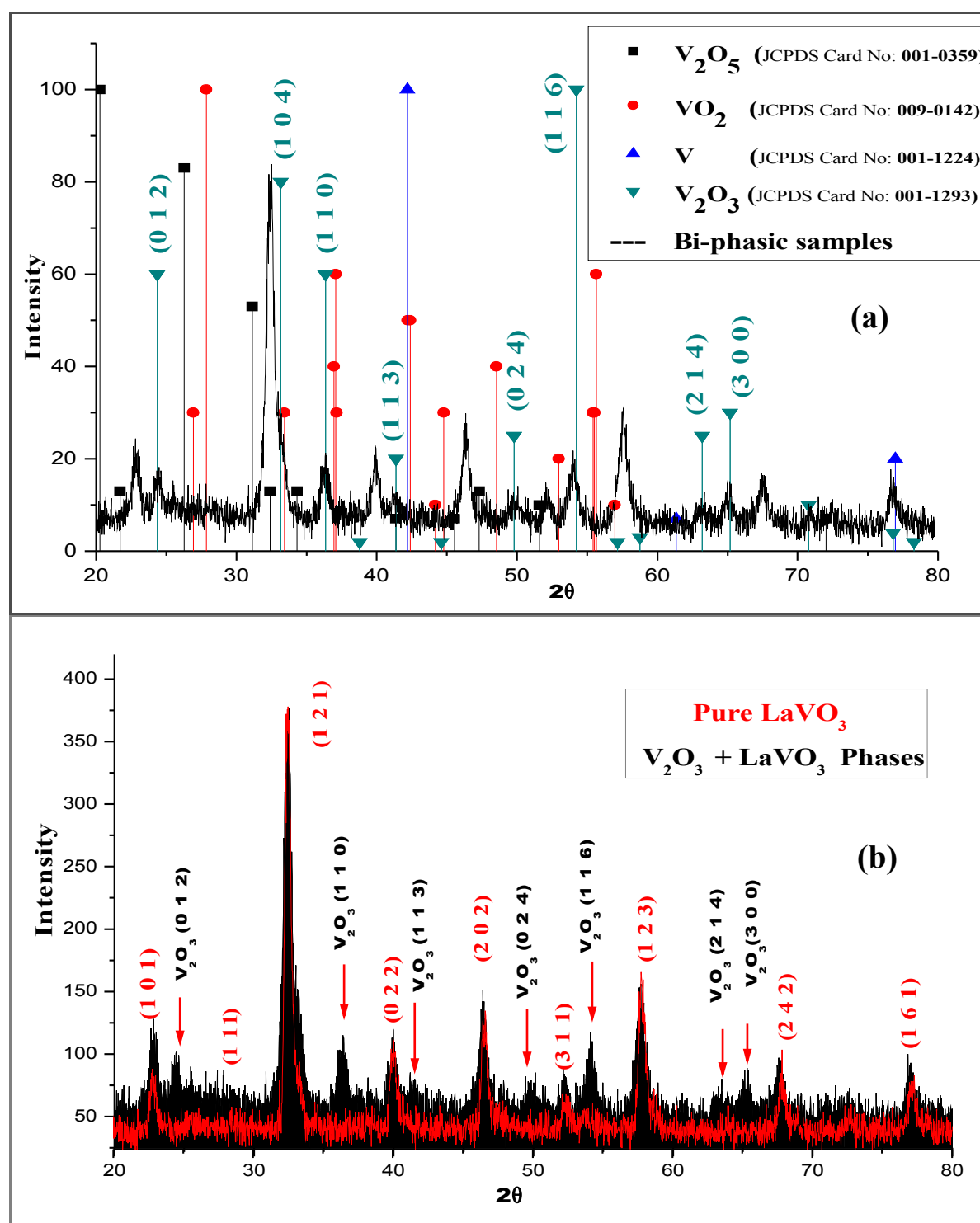| Sample Name	a(Å)	b(Å)	c(Å)	Volume (Å^3)
LaVO$_3$	5.528(2)	7.827(7)	5.531(1)	239.313(4)
La$_{0.96}$Bi$_{0.04}$VO$_3$	5.538(1)	7.834(5)	5.539(7)	240.307(8)
La$_{0.93}$Bi$_{0.07}$VO$_3$	5.541(5)	7.850(2)	5.547(2)	241.277(2)

Table 4.2 Lattice parameters of pure and doped samples.

Sample Name	a(Å)	b(Å)	c(Å)	Volume (Å^3)
0.66 LaVO$_3$ +	5.549(5)	7.828(2)	5.539(3)	240.600(7)
0.34 V$_2$O$_3$	4.91(4)	4.91(4)	13.74(6)	330.705(8)
0.46 LaVO$_3$ +	5.549(4)	7.837(1)	5.544(2)	241.094(7)
54% V$_2$O$_3$	4.93(1)	4.93(1)	13.97(6)	339.82(3)
26% LaVO$_3$ +	5.556(3)	7.844(1)	5.551(1)	241.919(5)
74% V$_2$O$_3$	4.96(2)	4.96(2)	13.95(2)	342.57(7)
Pure V$_2$O$_3$ by McWhan *et al.* [56]	4.95	4.95	14	343.04

Table 4.3 Lattice parameters of bi-phasic samples.

Magnetization measurements were accomplished for all samples by using MPMS to study the magnetic properties of samples with exact control of the sample temperature in the range of 5 to 300 K. The applied magnetic field of H=5 kOe was used. Magnetization results are presented as a mass magnetization versus temperature for all samples from Fig. 4.14 to Fig. 4.18. The inverse susceptibility versus temperature is also plotted in Fig. 4.19 to calculate the magnetic parameters for each sample. The values of the Néel temperature T_N, antiferromagnetic Curie temperature Θ, and the effective magnetic moment μ_{eff} for all samples are listed in Table 4.4 and Table 4.5.

The M-T curve for $LaVO_3$, shown in Fig. 4.14 exhibits a cusp peak at 140 K. The magnetization is not infinite at this temperature. The temperature dependence of magnetization above this temperature is paramagnetic. Therefore, the alignment of magnetic moments are randomized and the magnetization decreases with increasing thermal energy. Below 140 K the spin interactions start to align the magnetic moments anti-parallel to each other in two different sub-lattices which can cancel out gradually. This interaction leads the magnetization to become almost zero at low temperature. This indicates that $LaVO_3$ has a transition point from antiferromagnetic-to-paramagnetic behavior which is called Néel temperature (T_N). The antiferromagnetic behavior in $LaVO_3$ arises due to the increasing superexchange interaction between V-O-V bonds, as proposed by Goodenough and coworkers [9], as discussed in Section 2.2.2. This interaction leads to the localization of magnetic moment at t_{2g}^2 configuration as the bond angle of V-O-V increases [9]. The different magnetic parameters of $LaVO_3$ were calculated and given in Table 4.4. the effective magnetic moment (μ_{eff}) of the Curie-Weiss paramagnetic susceptibility is 3.82 μ_B. This value is different in comparison to the effective magnetic moment of a spin only (V^{3+}) 2.82 μ_B [25]. This difference is due to oxygen deficiency in $LaVO_3$ sample. The effective magnetic moment μ_{eff} = 3.82 μ_B, the Néel temperature of 140 K, and Curie temperature Θ = -710.5 K for $LaVO_3$ are in good agreement with the results of Goodenough *et al.* [9, 57], Mahajan *et al.* [18]*,* and Gharetape *et al.* [15]*,* respectively.

The experimental values for doped samples are also plotted in Fig. 4.14 and Fig. 4.16. The bend of plot of mass magnetization versus temperature and inverse susceptibility versus T are the characteristic feature of a antiferromagnetic to paramagnetic behavior. The transition temperatures of $La_{0.96}Bi_{0.04}VO_3$ and $La_{0.93}Bi_{0.07}VO_3$ samples decrease to $T_N = 137$ K and 136 K, respectively. By doping bismuth at La site, the local effect of the unpaired electrons $(6s^2)$ that are not bonded can change the interaction of the magnetic moments at V-O-V bonds, the Néel temperature decreases by three to four Kelvin and slightly decreases the net magnetization.

Magnetization curve for bi-phasic samples are given in Fig. 4.15 and Fig. 4.16. Presence of multiple phases in our samples are clearly reflected in their magnetic properties. Phase segregated compounds have two transition temperatures. The two kink points at 140 and 170 K are related to the transition temperature of $LaVO_3$ phase [18] and V_2O_3 phase [54, 58], respectively. The second transition temperature that expects to be for the V_2O_3 phase (XRD results section 4.2), was also verified with the measurement of Kosuge [54] as illustrated in Fig. 4.13. The magnetization versus temperature measurements (M-T curve) can be considered as a technique to identify phases in multiphasic samples which is more accurate and easier than x-ray diffraction method [54]. The combined magnetic moments of $LaVO_3$ and V_2O_3 cause net magnetization. A transition at Néel temperature (170 K) for V_2O_3 phase exhibits the changes of physical properties, which affects magnetic properties [58]. Surprisingly, the value of Θ for the bi-phasic samples, as tabulated in Table 4.5, are significantly higher than that of $LaVO_3$ and V_2O_3. This difference arises either due to the extraneous reasons that are unknown to us at this point, or due to the possible vacancies or structural defects. The latter requires further probing of our samples with techniques such as transmission electron microscope.

Mass magnetization at low temperature (5 K<T<65 K) are shown in Fig. 4.16 and Fig. 4.18 for pure $LaVO_3$, the magnetization is independent of temperature, but for doped and bi-phasic samples, the magnetization increases by decreasing temperature. This increase is purely arise from the paramagnetic behavior of $LaVO_3$ in case of oxygen deficiency at low temperature [18].

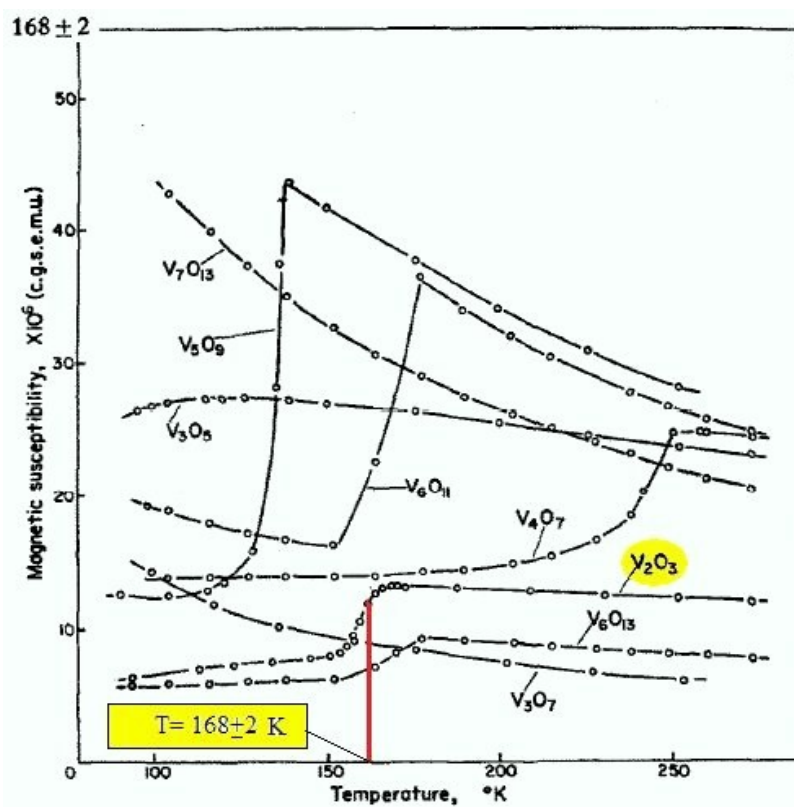Figure 4.13 Temperature dependence of magnetic susceptibility of vanadium oxides V_nO_{2n-1} (Magnéli phases), adopted and modified from Ref. [54].
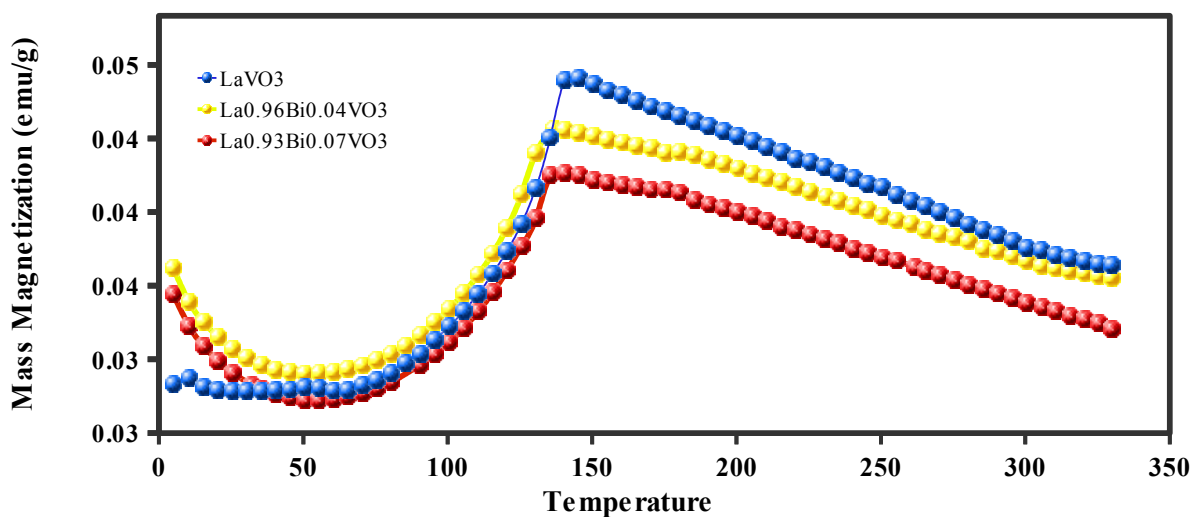
Figure 4.14 Temperature dependence of the mass magnetization of $La_{1-x}Bi_xVO_3$ at H=5 kOe, in temperature range of 4 K to 330 K.
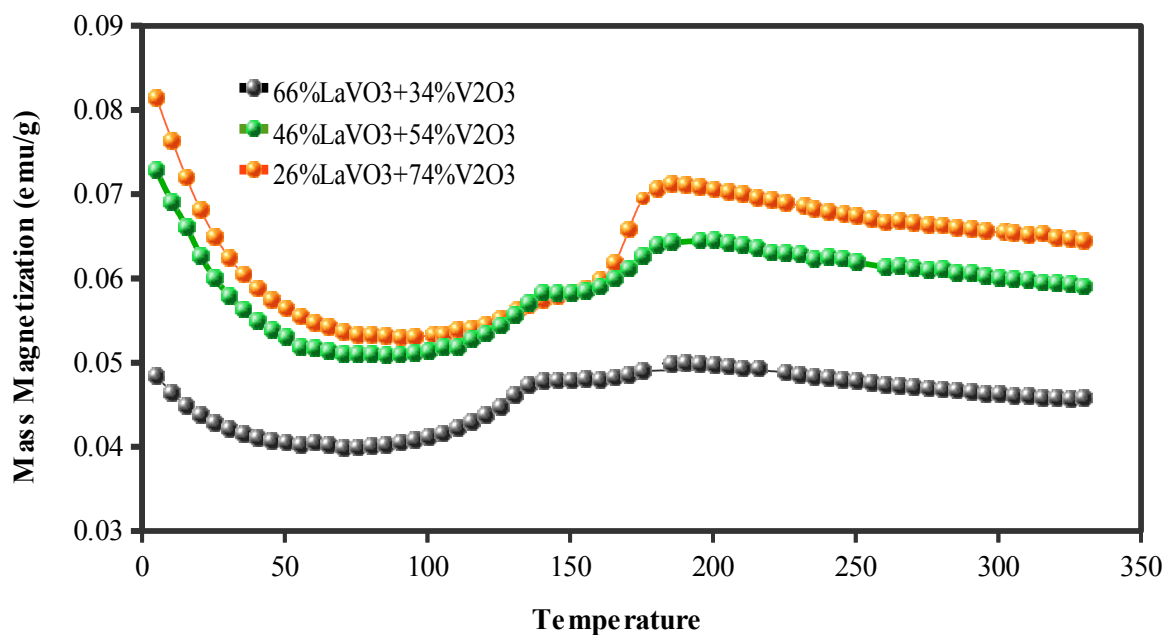

Figure 4.15 Temperature dependence of the mass magnetization of bi-phasic samples at H=5 kOe in temperature range of 4 K to 330 K.
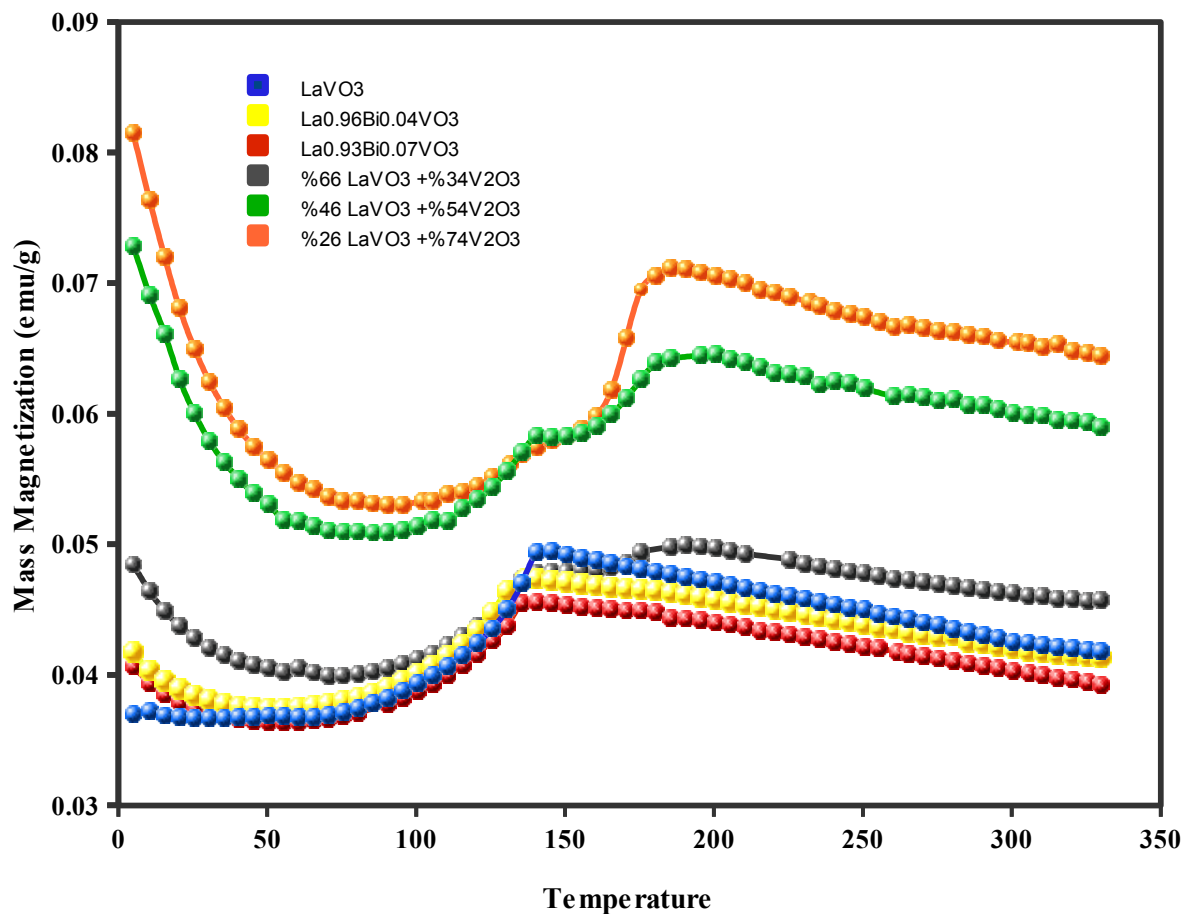
Figure 4.16 Mass magnetization versus temperature for all samples, showing a transition temperature at 140 K for LaVO$_3$, 137 K, and 136 K for doped samples. Two transition temperatures at 140 K and 170 K are measured for bi-phasic samples.
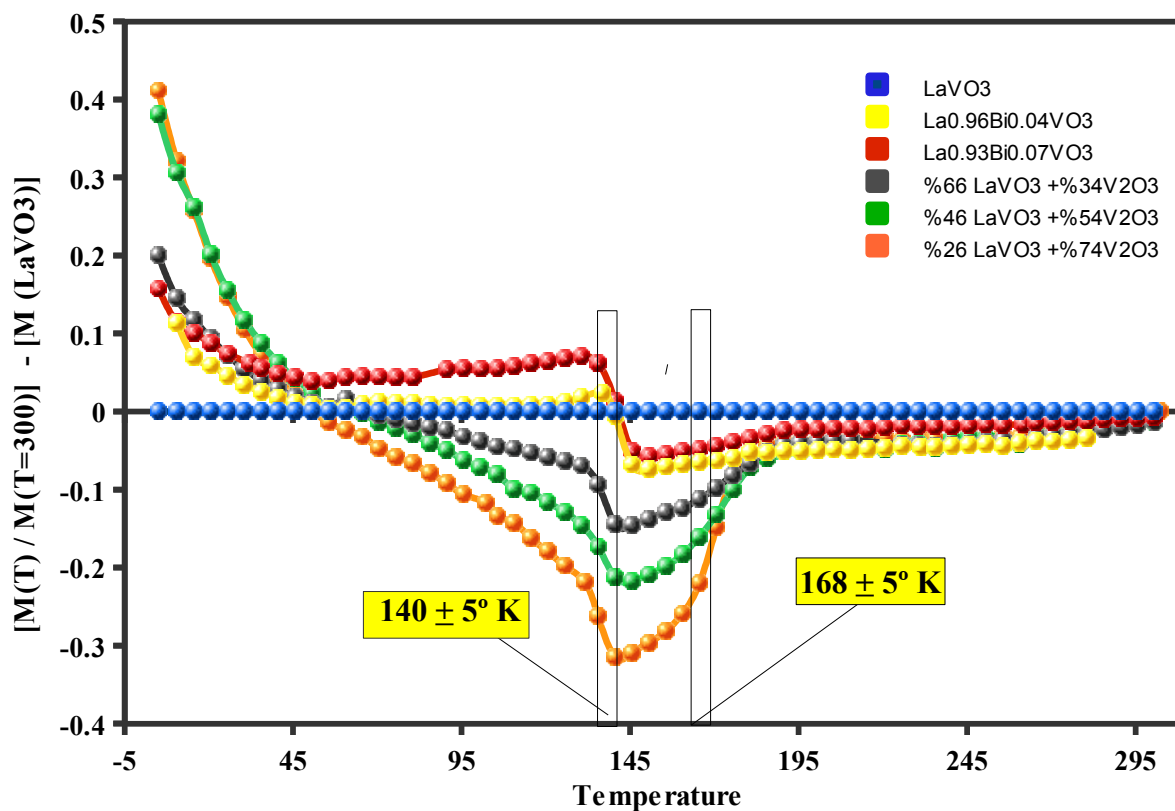
Figure 4.17 Normalized mass magnetization versus temperature for all samples in which to find exact transition temperatures (Néel temperature T_N), showing two transition temperatures around $T_N = 140 \pm 5$ K for $LaVO_3$ and $T_N = 168 \pm 5$ K for V_2O_3 phases.
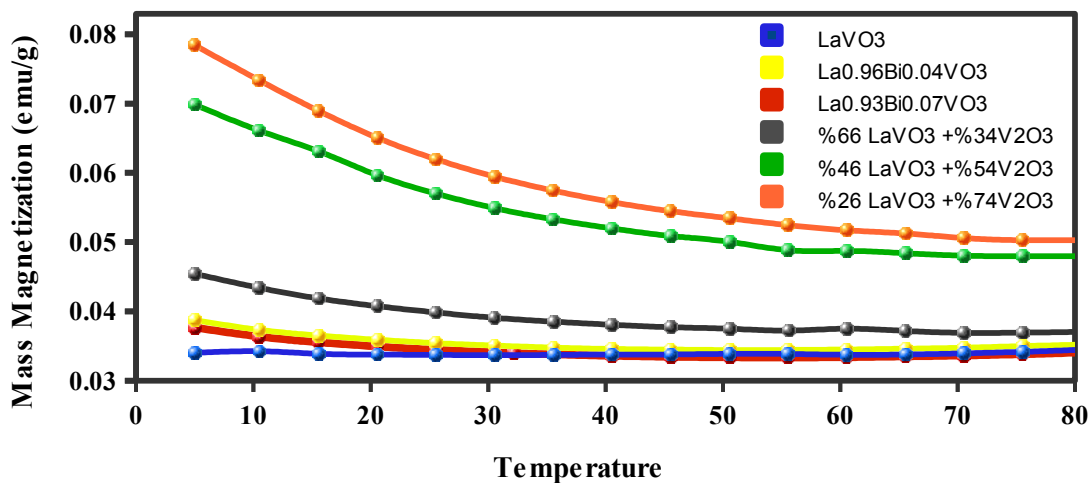
Figure 4.18 Mass magnetization at low temperature of all samples (5 K<T<65 K) shows paramagnetic behavior.

Figure 4.19 (a) Inverse mass susceptibility versus temperature for all the samples (b) Linear fittings above Néel temperature (T_N=140 K and 170 K) show the Curie-Weiss temperature values (Θ<0) of the samples at the intercept points.

Sample	C_g (emu.K. g^{-1})	Θ (K)	T_N (K)	μ_{eff} (μ_B)
LaVO$_3$	7.6441E-03	-710.5	140	3.819
La $_{0.96}$ Bi $_{0.04}$ VO$_3$	8.0373E-03	-785.6	137	3.913
La $_{0.93}$ Bi $_{0.07}$ VO$_3$	8.2515E-03	-865.1	136	3.965

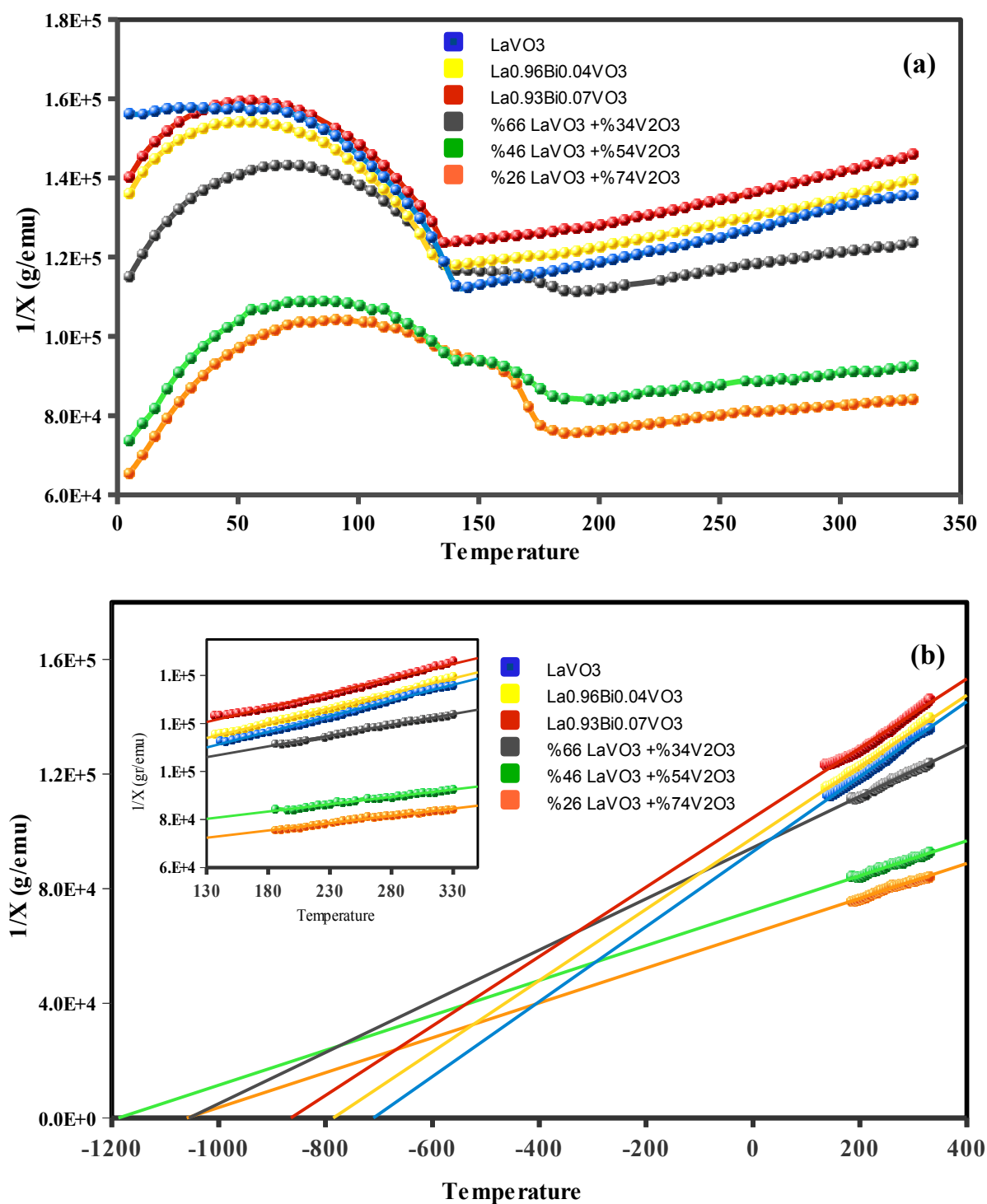Table 4.4 Calculation of Curie-constant (C_g), Curie-Weiss temperature (Θ), transition temperature (T_N), and effective magnetic moment for pure and doped samples.

Sample	C_g (emu.K.g^{-1})	Θ (pure LaVO$_3$) = **-710.5** K	Θ (pureV$_2$O$_3$) = **-720** K[54]	T_N (K)
		Θ_{Total} (K)		
66% LaVO$_3$+ 34% V$_2$O$_3$	1.12E-002	-1055.9		140 & 168$\pm$2
46% LaVO$_3$+ 54% V$_2$O$_3$	1.64E-002	-1187.6		140 & 168$\pm$2
26% LaVO$_3$+ 74% V$_2$O$_3$	1.64E-002	-1059.9		140 & 168$\pm$2

Table 4.5 Calculation of Curie-constant (C_g), Curie-Weiss temperature (Θ), and transition temperature (T_N) for bi-phasic samples.

The temperature dependence of resistivity (ρ) was measured from T = 70 to 350 K by PPMS for all samples as explained at Section. 3.5. For all samples, the resistivity is low at high temperature. But as the temperature decreases, the resistivity increases drastically (Fig. 4.21). The inset graph of Fig. 4.21 represents the Ln(ρ) as a function of temperature. Ln(ρ) versus reciprocal temperature curves are plotted in Fig. 4.22 then replotted in inset graph of Fig. 4.22 from 250 to 350 K to calculate the activation energy by linear fitting of Ln(ρ) versus 1/T curves. The value obtained for activation energy of the samples are given in Table 4.6.

For pure $LaVO_3$, ρ-T curve indicates the low resistivity at high temperature, but it increases sharply around transition temperature of $LaVO_3$. The localization of d spin in sub-lattices increases by decreasing temperature. The decreasing of the resistivity for $LaVO_3$ by increasing temperature is accompanied with the delocalization of the t_{2g}^2 electron at unfilled $3d^2$ shells of vanadium ions [27]. The gradual transition from intrinsic to localized electronic behavior leads the $LaVO_3$ to be semiconductor or "Mott" insulator as discussed in Section 2.3 [9]. The activation energy was calculated and given in Table 4.6. The value of E_a =0.11 eV for $LaVO_3$ is in agreement with the previous works done for this compound [16, 35].

As the doping increases in $LaVO_3$, the variation of resistivity with temperature has a similar behavior with pure $LaVO_3$, as shown in Fig. 4.21. But the resistivity of $La_{1-x}Bi_xVO_3$ samples increases with decreasing temperature at lower temperature than $LaVO_3$. The activation energy slightly decreases by doping bismuth at La site as given in Table 4.6. Bismuth substitution in the La site changes the activation energy and the resistivity. Generally, the chemical substitution gives distortion to the lattice and delocalizes d spins of V-O-V bonds at doping site [59]. Bismuth ions (Bi^{3+}) have an electron configuration $6s^2$ with two electrons that are not bonded. The exchange interaction energy between the bismuth $6s^2$ and vanadium $3d^2$ orbital can be a main reason for increasing the electrical conductivity of the doped samples at higher temperature in comparison to the pure one [27].

The electrical resistivity measured as a function of the temperature for the composite samples with V_2O_3 and $LaVO_3$ phases is shown in Fig. 4.21. We can see a slight discontinuity at $Ln(\rho)$ versus $1/T$ graph (Fig. 4.22) for the samples with 34% and 54% of V_2O_3 phase. This discontinuity become sharper for 74% V_2O_3 sample. Comparing resistivity behavior of 74% V_2O_3 sample with the pure V_2O_3 predict the similar metal-insulator transition as reported by Kuwamoto *et al.* [60] and McWhan *et al.* [61] shown in Fig. 4.20. The metal-insulator and phase transitions of V_2O_3 are accompanied with the spin and orbital dependence of the 3d-3d Coulomb energy [62] and a simultaneous change in the structural transition by temperature [62, 63]. The curvature of $Ln(\rho)$-$1/T$ graph increases with enhancing V_2O_3 phase, because the 3d-3d Coulomb energy of V-V bonds increases. This energy is an important reason for metal-insulator transition [64].
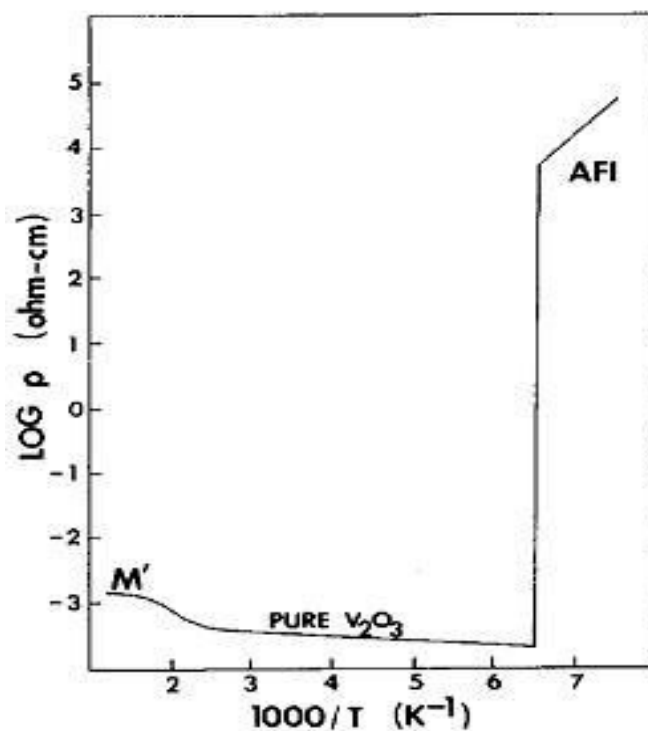

Figure 4.20 Log of resistivity versus reciprocal temperature for pure V_2O_3, showing a metal-insulator transition as a function of temperature, adopted from Ref. [60].
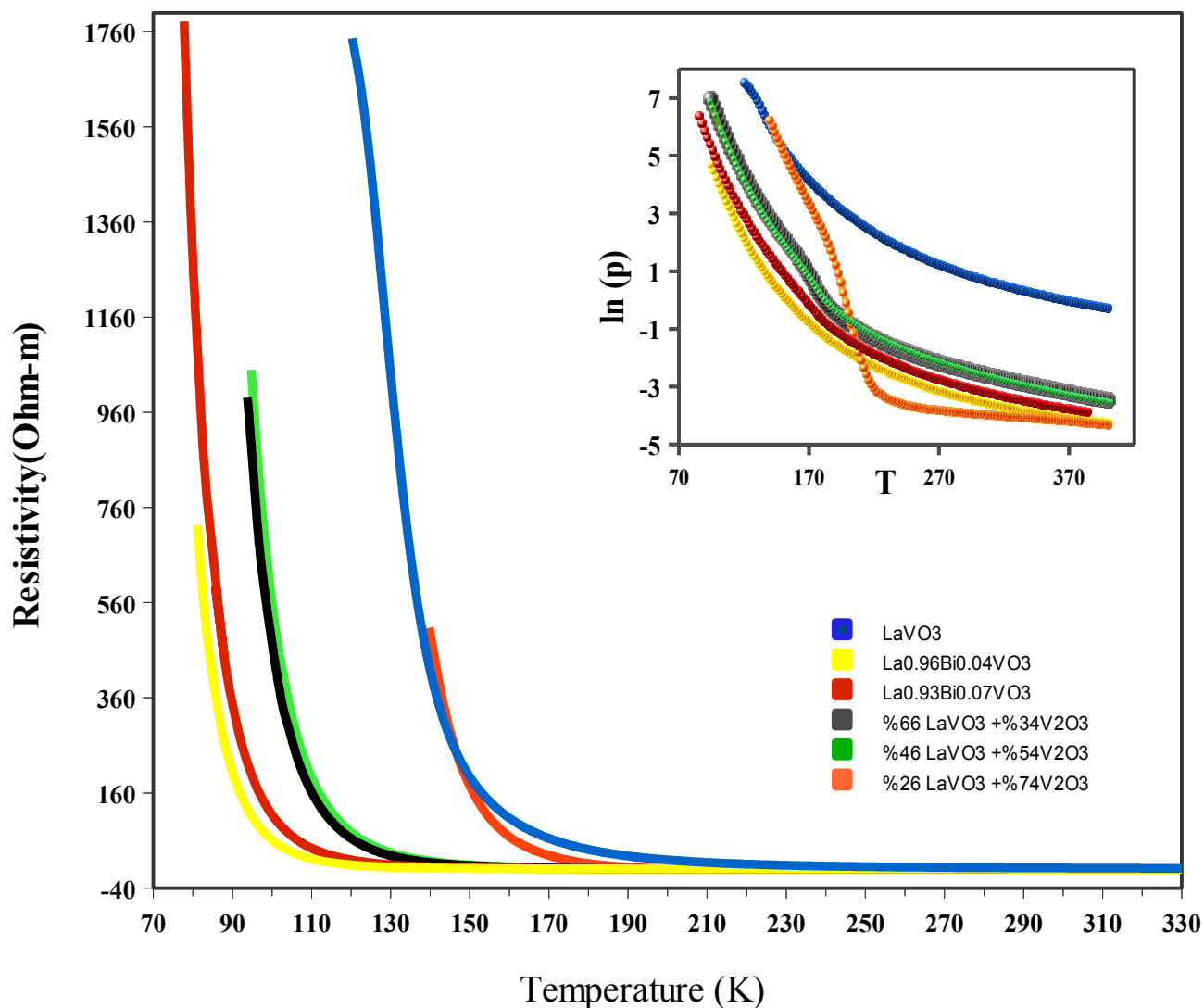
Figure 4.21 Resistivity measurement versus temperature (70 - 400 K) of $La_{1-x}Bi_xVO_3$ (x= 0, 0.04, 0.07) and bi-phasic samples of $(x)LaVO_3+(1-x)V_2O_3$ phases (x=0.66, 0.46, 0.26).
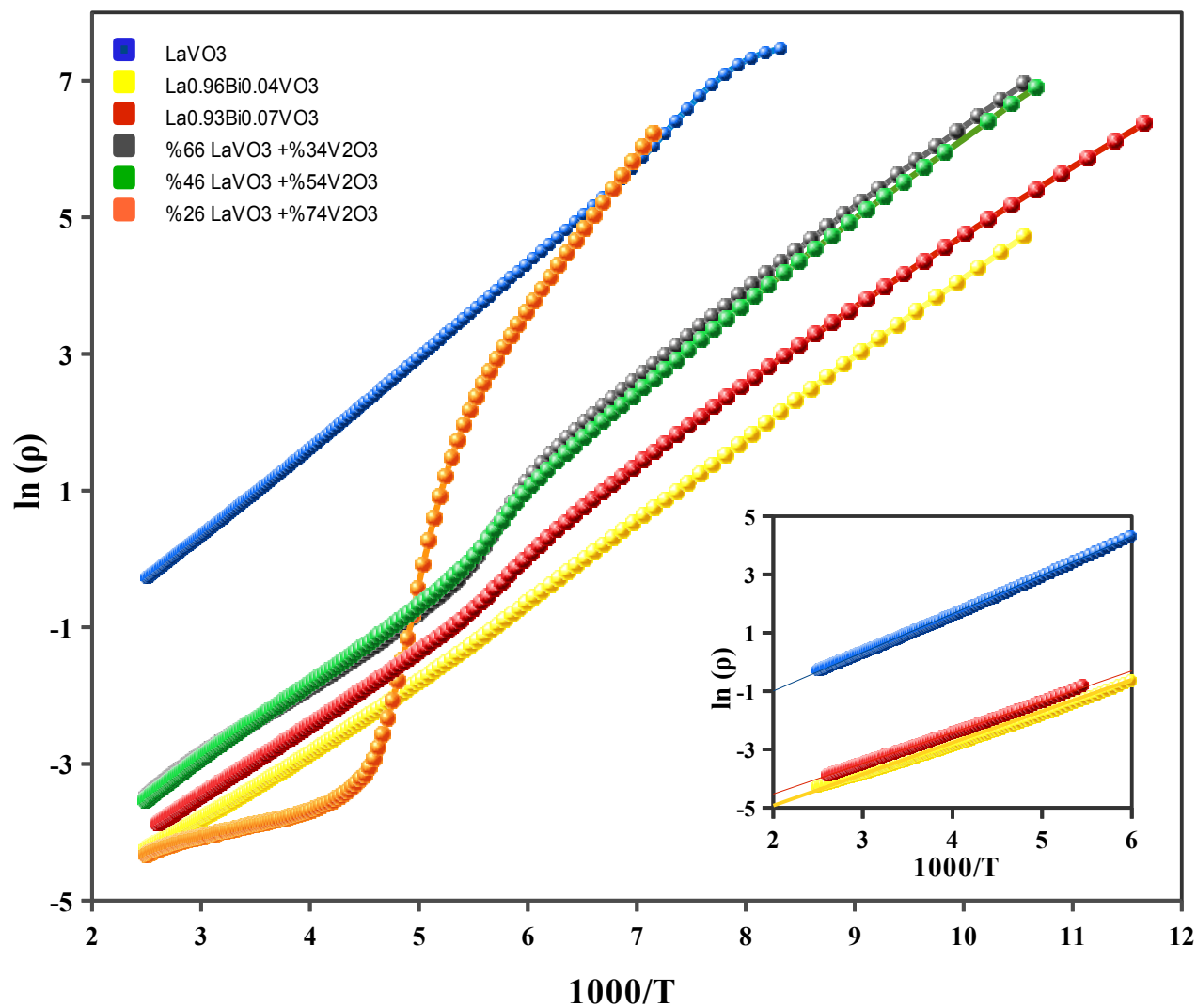
Figure 4.22 The graph of ln(ρ) versus 1000/T in the temperature range 50-400 K. The pure and the doped samples show linear behavior but bi-phasic samples show electrical transition from metallic to insulator. This is especially noticeable for the 74% V_2O_3 sample. The inset shows the linear fitting for pure and doped samples. This fitting at high-temperature is used in order to calculate activation energy in the range of 250 - 400 K.

X	Equation	E_a (eV)
0.000	$\ln(\rho) = 1.323\ (1000/T) - 3.635$	0.114
0.040	$\ln(\rho) = 1.080\ (1000/T) - 7.085$	0.0931
0.070	$\ln(\rho) = 1.055\ (1000/T) - 6.634$	0.091

Table 4.6 Activation energy of pure $LaVO_3$ and $La_{1-x}Bi_xVO_3$ samples was obtained from Ln of Arrhenius equation (Eqn. 3.3).

Chapter 5

Conclusions:

In this project, we successfully synthesized $LaVO_3$ and Bi-doped $LaVO_3$ polycrystalline samples. We studied the crystallinity, magnetic, and electrical properties of these samples with a specific focus on the impact of Bi-doping in $LaVO_3$. We attempted to substitute bismuth with high percentage at La site; however, we were only successful for substitution of less than ten percent Bi. Bismuth was an interesting doping candidate because the effect of unpaired (lone-pair) $6s^2$ electrons decreased the transition temperature. It is to be noted that the difficulties of the preparation of $La_{1-x}Bi_xVO_3$ samples might lead to the further work in order to to achieve a higher percentage of Bi-doping of $La_{1-x}Bi_xVO_3$ samples. The synthesis condition used in this work might be modified through the lower annealing temperature or a variation of annealing time. Alternative synthesis methods may be required to obtain a single phase $La_{1-x}Bi_xVO_3$ for $x > 0.1$.

The parent and the doped samples were found to exhibit the orthorhombic distortion at room temperature, which were characterized by XRD measurements. In bi-phasic samples, the orthorhombic and hexagonal symmetries were characterized for $LaVO_3$ and V_2O_3 phases, respectively. We confirmed the two magnetic transitions for bi-phasic samples, one at T_N=140 K for $LaVO_3$ and the second one at T_N=170 K for V_2O_3.

Magnetic properties measurement using SQUID magnetometer showed the paramagnetic to antiferromagnetic transition for all samples. We confirmed the magnetic transitions (Néel temperature) at 140 K for $LaVO_3$, however, this temperature was dropped to 137 K for $La_{0.96}Bi_{0.04}VO_3$ and 136 K for $La_{0.93}Bi_{0.07}VO_3$. The two magnetic transition temperatures, one at T_N=140 K and another at T_N=170 K, were identified in bi-phasic samples with $LaVO_3$ and V_2O_3 phases, respectively.

The resistivity results showed a semiconductor behavior for all samples that was observed by four probe resistivity measurement. The activation energy decreased slightly from 0.11 to 0.09 eV for pure and doped samples. The discontinuity in log of resistivity versus inverse temperature graph manifested a metallic to insulator transition for the sample with 74% V_2O_3.

References

1. Y. Ren, A.A. Nugroho, A.A. Menovsky, J. Strempfer, U. Rutt, F. Iga, T. Takabatake and C.W. Kimball, Phys. Rev. B. **67**, 014107 (2003).

2. N.A. Spaldin, "Magnetic Materials Fundamentals and Device Applications", Cambridge University Press,42-60, (2006).

3. G.F. Dionne, "Magnetic Oxides", Springer Science and Business Media, 10-120 (2009).

4. M.J. Martínez-Lope, J. A. Alonso, M. Retuerto, and M. T. Fernández-Díaz, Inorg. Chem. **47**, 2634 (2008).

5. J.-S. Zhou,1, J.B. Goodenough, J.-Q. Yan, J.-G. Cheng, K. Matsubayashi, Y. Uwatoko, and Y. Ren, Phys. Rev. B **80**, 224422 (2009).

6. J.-S. Zhou and J.B. Goodenough, Phys. Rev. Lett, **99**, 156401 (2007).

7. M. Reehuis, C. Ulrich, P. Pattison, B. Ouladdiaf, M.C. Rheinstadter, M. Ohl, L.P. Regnault, M. Miyasaka, Y. Tokura, and B. Keimer, Phys. Rev. B **73**, 094440 (2006).

8. S. Miyasaka1, Y. Okimoto, M. Iwama, and Y. Tokura, Phys. Rev. B **68**, 100406 (2003).

9. J.B. Goodenough, "Localized to Itinerant Electronic Transition in Perovskite Oxides", Springer Science and Business Media, 3-40 (2001).

10. P. Bordet, C. Chaillout, M. Marezio, Q. Huang, A. Santoro, S-W. Cheong, H. Takagi, C.S. Oglesby and B. Batlogg, J. Solid State Chemistry. **106**, 253 (1993).

11. F. Inaba, T. Arima, T. Ishikawa, T. Katsufuji and Y. Tokura, Phys. Rev. B. **52**, R2221 (1995).

12. M. Onoda and H. Nagasawa, Solid State Communications. **99**,487 (1996).

13. H. Seim and H. Fjellvag, Acta Chemica Scandinavia, **52**, 1096 (1998).

14. H. Seim, H. Fjellvag and B.C. Hauback, Acta Chemica Scandinavia. **52**, 1301 (1998).

15. S.J. Gharetape, M.P. Singh, F.S. Razavi, D.A. Crandles, L.Y. Zhao and K.T. Leung, Appl. Phys. Lett. **98**, 052509 (2011).

16. K. Maiti, N.Y. Vasanthacharya and D.D. Sarma, J. Phys. Condens. Matter. **9**, 7507

(1997).

17.   P. Dougier and P. Hagenmuller, J. Solid State Chem. **15**, 158 (1975).

18.   A.V. Mahajan, D.C. Johnston, D.R. Torgeson and F. Borsa, Phys. Rev. B. **46**, 10973 (1992).

19.   I. Chaitanya Lekshmi, A. Gayen and M.S. Hegde, J. Phys. Chem. Solid. **66**, 1647 (2005).

20.   W. Choi, T. Sands and K,-Y. Kim, J. Mater. Res. **15**, 1 (2000).

21.   T.M. Dao, P.S. Mondal, Y. Takamura, E. Arenholz, and J. Lee, Appl. Phys. Lett. **99**, 112111 (2011).

22.   CRC handbook of Chemistry and Physics, 92nd Edition, 2011-2012 (R.D Shannon, Acta Crystallogr. **A32**, 751 (1976) and Y.Q. Jia, J. Solid State Chem. **95**, 184 (1991).

23.   J. Geck, P. Wochner, S. Kiele, R. Klingeler, A. Revcolevschi, M.V. Zimmermann, B. Büchner and P. Reutler, New J. Phys. **6**,152 (2004).

24.   R. Gautreau and W. Savin, "Theory and Problems of Modern Physics", McGraw-Hill, second   edition, 122-160, (1999).

25.   C. Kittel, "Introduction to Solid State Physics", 7th edition, John Wiley India Edition, 150-180, 442-470 (2007).

26.   A. Gafner, "Construction of NMR equipment to be used in the Physical Properties Measurement System." (PPMS, Quantum Design), University of Zurich, (2006).

27.   P.A. Cox, "Transition Metal Oxide an Introduction to their Electronic Structure and Properties", Oxford Science Publications, 150-230 (1992).

28.   J.K. Furdyna, N. Samarth, R.B. Frankel, and J. Spalek, Phys. Rev. B. **37**, 3707 (1988).

29.   M. Mcelfresh, "Fundamentals of Magnetism and Magnetic Measurements", Quantum Design Support, 15-25 (1994).

30.   N.W. Ashcroft, N.D. Mermia,"Solid State Physics", Saunders College Publishing, 685-690 (1976).

31.   R.J.O. Mossanek, M. Abbate, P.T. Fonseca, A. Fujimori, H. Eisaki, S. Uchida,

and Y. Tokura, Phys. Rev. B. **80**, 195107 (2009).

32. J.M.D. Coey, "Magnetism and Magnetic Materials", Cambridge University Press, (2010).

33. N.F. Mott, "Metal-Insulator Transitions", second edition, Taylor & Francis, Chapter 4 (1990).

34. W.R. Runyan and T.J. Shaffner, "Semiconductor Measurements & Instrumentation", 2nd edition, McGraw-Hill, Chapter 4 and 11 (1997).

35. C.P. Khattak and F.F.Y, Wang, "Handbook on The Physics and Chemistry of Rare-earths", North-Holland Physics Publishing,Volume 3, 525 (1984).

36. Y.A. Firsov, "Polarons in Advanced Materials", Springer Series in Materials Science, Volume **103**, 63 (2007).

37. M. Okutan, H.I. Bakan, Kemal, Korkmaz, F. Yakuphanoglu, Physica B. **355**, 176 (2005).

38. D.B. McWhan and J.P. Remeika, Phys. Rev. B. **2**, 3734 (1970).

39. L. Wang, "Microscopic Composition Measurement at Nanoscale", Data Strong System Center (DSSC) seminar, April (2005).

40. J. Goldstein, "Scanning electron microscopy and x-ray microanalysis", Kluwer Adacemic Plenum Pulbishers, 689 (2003).

41. C. Suryanarayana, M.G. Norton. "X-ray Diffraction, A Practical Approach". 207-221 (1998).

42. J.R. Connolly, "Introduction to X-Ray Powder Diffraction", Spring 2012.

43. SQUID Application Note 1052-202, Quantum Design, (2001).

44. J.B. Ketterson and S.N. Song, " Superconductiviy", Cambridge University Press, 75 (1999).

45. R.P. Giffard, R.A. Webb and J.C. Wheatley, "Principles and Methods of Low-Frequency Electric and Magnetic Measurements Using an rf-Biased Point-Contact Superconducting Device", J. Low Temp. Phys. **6**, 533 (1972).

46. J. Clarke and A.I. Braginski "The SQUID Handbook: Application of SQUIDs and SQUID Systems" Volume 2, Wiley-VCH, Chapter 13 (2006).

47. R. Brennan and D. Dickey, "Determination of diffusion characteristic using two-

and four-point probe measurements." Solid State Technology, 125-132 (1984).

48.   Physical Property Measurement System (PPMS), Quantum Design support, www.qdusa.com (2004).

49.   G. Herrera, E. Chavira, J. Jimenez-Mier, A. Ordonez, E. Fregoso-Israel, L. Banos, E. Bucio, J. Guzman, O. Novelo and C. Flores, Journal. Alloys and Compounds. **479**, 511 (2009).

50.   F. Krumeich et al. Eldgenossische Technische Hochschule Zurich (ETH), October (2010).

51.   T. Atou, H. Chiba, K. Ohoyama, Y. Yamaguchi, and Y. Syono, Journal of Solid State Chemistry, **145,** 639 (1999).

52.   K. Oka, M. Azuma, W.-T. Chen, H. Yusa, A.A. Belik, E. Takayama-Muromachi, M. Mizumaki, N. Ishimatsu, N. Hiraoka, M. Tsujimoto, M.G. Tucker, J.P. Attfield and Y. Shimakawa, J. Am. Chem. Soc. **132(27)**, 9438 (2010).

53.   S. Kachi and R. Roy, Second Quarterly Report on Crystal Chemistry Studies, Pennsylvania State University (1965).

54.   K. Kosuge, J. Phys. Chem. Solids. **28**, 1613 (1967).

55.   J.L.G. Fierro. "Metal Oxide Chemistry & Application". Taylor and Francis Group,167 (2006).

56.   D.B. McWhan, A. Menth, J.P. Remeika, W.F. Brinkman, and T.M. Rice, Phys. Rev. B **7**, 1920 (1973).

57.   V.G. Zubkov, G.V. Bazuev, V. A. Perelyaev, and G.P. Shveiken, Fiz. Tverd. Tela (Leningrad) **15**, 1610 (1973) [Sov. Phys. Solid State **15**, 1079 (1973)].

58.   J.M. Honig and L.L. Van Zandt, Phys. Rev. B. **6**, 1323 (1972).

59.   F. Arfat, African Physical Review. **3**, 29 (2009).

60.   H. Kuwamoto, J.M. Honig, J. App. Phys. Rev. B. **22**, 2626 (1980).

61.   D.B. McWhan and Remeika, J.P. Phys. Rev. B, **2**, 3734 (1970).

62.   P.D. Dernier and M. Marezio, Phys. Rev. B. **2**, 3771 (1970).

63.   P.D. Dernier, J. Phys. Chem. Solids. **31**, 2569 (1970).

64.   J.-H. Park, L.H. Tjeng, A. Tanaka, J.W. Allen, C.T. Chen, P. Metcalf, F.M.F. de Groot and G. A. Sawatzky, Phys. Rev. B. **61**, 11506 (2000).